

GALACTIC DISK WINDS DRIVEN BY COSMIC RAY PRESSURE

S. ALWIN MAO¹ AND EVE C. OSTRIKER¹

¹*Department of Astrophysical Sciences, Princeton University, Princeton, NJ 08544, USA*

ABSTRACT

Cosmic ray pressure gradients transfer energy and momentum to extraplanar gas in disk galaxies, potentially driving significant mass loss as galactic winds. This may be particularly important for launching high-velocity outflows of “cool” ($T \lesssim 10^4$ K) gas. We study cosmic-ray driven disk winds using a simplified semi-analytic model assuming streamlines follow the large-scale gravitational potential gradient. We consider scaled Milky Way-like potentials including a disk, bulge, and halo with a range of halo velocities $V_H = 50 - 300$ km s⁻¹, and streamline footpoints with radii in the disk $R_0 = 1 - 16$ kpc at height 1 kpc. Our solutions cover a wide range of footpoint gas velocity u_0 , magnetic-to-cosmic-ray pressure ratio, gas-to-cosmic-ray pressure ratio, and angular momentum. Cosmic ray streaming at the Alfvén speed enables the effective sound speed C_{eff} to *increase* from the footpoint to a critical point where $C_{\text{eff,c}} = u_c \sim V_H$; this differs from thermal winds in which C_{eff} *decreases* outward. The critical point is typically at a height of 1 – 6 kpc from the disk, increasing with V_H , and the asymptotic wind velocity exceeds the escape speed of the halo. Mass loss rates are insensitive to the footpoint values of the magnetic field and angular momentum. In addition to numerical parameter space exploration, we develop and compare to analytic scaling relations. We show that winds have mass loss rates per unit area up to $\dot{\Sigma} \sim \Pi_0 V_H^{-5/3} u_0^{2/3}$ where Π_0 is the footpoint cosmic ray pressure and u_0 is set by the upwelling of galactic fountains. The predicted wind mass-loss rate exceeds the star formation rate for $V_H \lesssim 200$ km s⁻¹ and $u_0 = 50$ km s⁻¹, a typical fountain velocity.

Keywords: galaxies: ISM – galaxies: star formation – galaxies: evolution – cosmic rays

1. INTRODUCTION

The study of galactic winds seeks to understand the loss of mass from galaxies. Mass loss through winds is believed to be responsible for substantially reducing the observed baryon mass fraction in galaxies below cosmic values, and for helping to quench ongoing star formation, especially in low-mass galaxies (e.g. Somerville & Davé 2015; Naab & Ostriker 2017). Many studies have concluded that only up to 10 – 20% of the cosmic baryons can be found in stars and gas within galaxies (e.g. Bell et al. 2003; Moster et al. 2013; Behroozi et al. 2013; Rodríguez-Puebla et al. 2017), and this fraction steeply drops off for halos either above or below $\sim 10^{12} M_\odot$. Except for the highest mass halos, the hot halo gas ($T \gtrsim 10^6$ K) does not appear to make up for the baryon deficit, but substantial warm ($T \sim 10^4$ K) and warm-hot ($T \sim 10^5 - 10^6$ K) gas is present in circumgalactic regions for a range of halo masses and redshifts, based on absorption-line surveys and other probes (e.g. Cen & Ostriker 1999; Anderson & Bregman 2010; Chen 2012; Putman et al. 2012; Werk et al. 2014; Prochaska et al. 2017). As accretion timescales are shorter than the Hubble time, circumgalactic gas that is accreted must subsequently be removed by galactic winds, and these winds are also presumably responsible for enriching the circumgalactic and intergalactic medium with metals (e.g. Tumlinson et al. 2017).

Direct evidence of winds from galaxies is given by high-velocity emission and absorption lines that probe gas at a wide range of temperatures (see Veilleux et al. 2005; Heckman & Thompson 2017, for reviews). Most observations of galactic outflows have focused on starburst systems, and indicate empirical scaling relations that have yet to be fully explained. Martin (2005) used Na I and K I absorption lines in ultra-luminous infrared galaxies to study cool gas outflows, finding that the outflow speed $v \propto \dot{M}_*^{0.35}$, where \dot{M}_* is the star formation rate. With Cosmic Origin Spectrograph *Hubble Space Telescope* data from 48 nearby star-forming galaxies, Chisholm et al. (2015) found that outflow velocities scale as $v \propto \dot{M}_*^{0.08-0.22}$, $v \propto M_*^{0.12-0.20}$, and $v \propto v_{\text{circ}}^{0.44-0.87}$, where M_* is the total stellar content and v_{circ} is the galaxy’s circular velocity. Chisholm et al. (2017) extended this analysis to explore correlations between outflow rates and galaxy properties for seven galaxies, finding a ratio of mass outflow rate to star formation rate $\dot{M}_{\text{wind}}/\dot{M}_* \equiv \beta$ (the “mass loading factor”)

$$\beta = 1.12 \pm 0.27 \left(\frac{v_{\text{circ}}}{100 \text{ km/s}} \right)^{-1.56 \pm 0.25}. \quad (1)$$

Work by Heckman et al. (2015) used ultraviolet absorption lines in 39 galaxies to study warm ionized starburst-driven winds. Heckman et al. (2015) found a slightly shallower power law for mass-loading than Chisholm et al. (2017), with best-fit $\beta \propto v_{\text{circ}}^{-0.98}$ for strong outflows, but their data are also roughly consistent with power laws slopes between -1 and -2 . Heckman & Borthakur (2016) found that outflow velocities scale roughly as $v \propto \dot{M}_*^{0.3}$ and $v \propto v_{\text{circ}}^{1.16 \pm 0.36}$. The variations among recent reported observations suggests that empirical wind scaling relations are not yet definitive, and it is uncertain how these may extend from starbursts to more normal star-forming galaxies.

Proposed theoretical mechanisms for driving galactic winds have been reviewed by Veilleux et al. (2005); Heckman & Thompson (2017). An important early galactic wind model, motivated by the iconic starburst M82, considers a hot, adiabatic radial flow that originates with specified mass and energy input rates within the central region of a starburst nucleus (Chevalier & Clegg 1985). The hot gas in models of this kind is assumed to be created by extremely high velocity shocks arising from stellar winds and supernovae. The asymptotic velocity of the gas in this model depends on the central gas temperature, which in turn depends on the (adopted) ratio of energy to mass input

rates. If an initially-hot wind of this kind has high enough energy loading to reach high velocity, but also mass loading in the regime that allows it to cool subsequent to acceleration, then radiative cooling by metal lines could in principle produce a high velocity warm or cold outflow (Wang 1995; Bustard et al. 2016; Thompson et al. 2016). However, there is only a limited range of mass-loading $\beta_{\text{hot}} \sim 1 - 2$ that allows a wind to cool strongly *after* accelerating to high velocity (Thompson et al. 2016), and it is not clear whether this range of β_{hot} is compatible with the detailed interaction between blast waves from multiple correlated supernovae and the surrounding interstellar medium (ISM). Kim et al. (2017) show that except in extreme events, superbubbles are expected to cool before breaking out of the surrounding ISM, and that the residual hot gas at the time of breakout has $\beta_{\text{hot}} \sim 0.1 - 1$. Kim & Ostriker (2017, submitted) found in self-consistent simulations (for Solar neighborhood conditions) with star formation and supernova feedback that $\beta_{\text{hot}} \sim 0.1$ above $z \sim 1$ kpc, and the hot, high-velocity outflow remains adiabatic.

Another mechanism that has been proposed for driving a high-velocity warm outflow is that a hot, high-velocity flow transfers momentum to embedded warm (or even cold), dense clouds. A longstanding difficulty with this cloud entrainment model, however, is that significant acceleration of clouds is generally accompanied by cloud shredding and destruction on short timescales (e.g. Scannapieco & Brüggén 2015; Zhang et al. 2017b, and references therein). Acceleration of individual dense clouds by radiation pressure forces similarly tends to destroy them (e.g. Proga et al. 2014; Zhang et al. 2017a).

Cosmic rays are believed to be accelerated in the shocks created by supernovae, with $\sim 10\%$ of the injected energy going into cosmic rays, and the local energy density of cosmic rays comparable to other energy densities in the Milky Way’s interstellar medium (e.g. Bell 2004; Grenier et al. 2015). GeV particles, which represent the largest contributor to the cosmic ray energy density, are confined within the galaxy for only ~ 10 Myr, and in flowing out of the galaxy they interact via the magnetic field with the ISM gas (e.g. Zweibel 2017). Cosmic ray pressure gradients transfer momentum (and energy) from the cosmic rays to the gas, and may help to drive galactic winds. In this paper, we focus on analyzing the capability of cosmic ray-gas interactions to accelerate cool ($T \sim 10^4$ K) gas to high velocities such that it is able to escape far into galactic halos.

The first studies of a cosmic-ray-driven galactic wind were by Ipavich (1975). He found that cosmic rays can drive galactic winds with mass loss rates of $1 - 10M_{\odot}/\text{yr}$, and that even zero temperature gas can be accelerated. A limitation of this exploratory study was that the framework adopted was a spherical, Keplerian potential in analogy to the solar wind. As we shall show, the form of the gravitational potential significantly affects the character of winds, and in particular the potential associated with an extended mass distribution in galaxies leads to constraints and types of wind solutions that are quite different from those for a Keplerian potential.

Further studies by Breitschwerdt et al. (1991) incorporated a more realistic galactic potential (Miyamoto-Nagai bulge-disk and dark matter halo), and adopted the (arbitrary) assumption of vertical streamlines in which the cross-sectional area varies as $A(z)/A_0 = 1 + (z/Z_0)^2$. They focused on non-radiative gas, and allowed for nonzero wave pressure. From their sampling of parameter space, they found that cosmic rays were necessary to drive a wind in many cases (except for very high initial temperature), and in particular, for typical conditions in the Milky Way galaxy. Cases with large initial (combined) energy density led to the highest mass-loss rates, and higher initial density tended to reduce the mass-loss rate. Recchia et al. (2016) solved similar equations to Breitschwerdt et al.

(1991), except that they assumed waves are fully damped, while allowing for nonzero diffusivity that is self-consistently calculated based on the wind solution.

Everett et al. (2008), motivated by diffuse X-ray observations towards the inner Galaxy, studied winds driven by a combination of cosmic ray and thermal pressure. They found that cases with cosmic ray pressure comparable to the thermal gas pressure produced the best fit to the observed Galactic diffuse soft X-ray emission. Their models indicate that thermal pressure imparts momentum and energy to the flow early on, and is more effective than cosmic ray pressure in mass-loading a wind. The terminal velocity and the evolution of the wind further from the base is more sensitive to the cosmic ray pressure. For fixed total (cosmic ray plus thermal) footpoint pressure, Everett et al. (2008) find that predominantly thermal-driven winds have higher mass-loss rates than predominantly cosmic-ray-driven winds. However, high thermal pressure is not guaranteed, and other work finds that the pressure of hot gas in the wind-launching region at $z \sim \text{kpc}$ is insufficient to drive strong disk winds in typical star-forming galaxy environments (Kim & Ostriker 2017, submitted).

In addition to idealized analytic models, three-dimensional hydrodynamic and magnetohydrodynamic (MHD) simulations have recently been performed to explore the role of cosmic ray pressure forces in driving galactic outflows. These have adopted varying assumptions concerning the treatment of cosmic rays. For example, Uhlig et al. (2012) do not include diffusion or MHD, and assume that the cosmic ray fluid streams at the sound speed along the direction of the cosmic ray pressure gradient; Hanasz et al. (2013) and Simpson et al. (2016) neglect streaming of the cosmic ray fluid relative to the gas but include advection at the gas velocity and adopt fixed diffusion coefficients parallel and perpendicular to the magnetic field; Booth et al. (2013) and Salem & Bryan (2014) and Salem et al. (2014) neglect cosmic ray streaming and MHD, adopting an isotropic diffusivity; Ruszkowski et al. (2017) compare models in which cosmic rays stream along the cosmic ray pressure gradient at a speed proportional to the Alfvén speed or diffuse parallel to the magnetic field. All of these simulation studies have found that cosmic ray pressure gradients can drive significant winds, with mass-loss rates that can be comparable to star formation rates but are dependent on the detailed prescription and parameters adopted. A notable feature of simulations with a cosmic ray fluid is that galactic winds include cool ($T \lesssim 10^4$ K) gas.

In this paper, we extend steady state one-dimensional studies of cosmic-ray driven winds to consider the case in which thermal pressure is negligible. We are motivated by observations that suggest high-velocity cool winds are ubiquitous (including even molecular gas), while at the same time simulations suggest that Type II supernovae interacting with the ISM produce hot gas at a rate $\dot{M}_{\text{hot}}/\dot{M}_* = \beta_{\text{hot}} \lesssim 1$; taken together, this argues that heavily mass-loaded winds ($\beta > 1$) must rely on acceleration of warm and cold (rather than hot) ISM phases to speeds exceeding $\sim v_{\text{circ}}$ that allow escape. Thermal pressure is included in our models by an isothermal equation of state with $c_s = 10 \text{ km s}^{-1}$, and it plays no role in wind acceleration. Although we do not explicitly follow the ionization level in the gas, we implicitly assume that this is high enough for the gas to be well-coupled to the magnetic field; for the low-density extraplanar warm medium under consideration, photoionization is believed to dominate (e.g. Ferrière 2001; Haffner et al. 2009). We do not include cosmic ray diffusion or explicit wave pressure, assuming that the cosmic ray fluid streams at the Alfvén speed relative to the gas. As in previous one-dimensional models, the streamline shape and cross-sectional area are prescribed, but our choices for these follow from the galactic potential rather than being arbitrary. We integrate the wind equation along streamlines to obtain the gas velocity, density, magnetic field,

and cosmic ray pressure, seeking solutions that make smooth transitions through a sonic point. To complement our numerical solutions, we obtain analytic scaling relations for the properties of winds.

In § 2 we describe our assumptions and mathematical formulation (§ 2.1, § 2.2), derive a one-dimensional steady wind equation (§ 2.3), discuss the critical point transition and our integration method (§ 2.4), and connect to a form of the Bernoulli equation (§ 2.5). Section 3 contains our results. We specify the details of our galactic models and input parameterization (§ 3.1), give examples of wind solutions for dwarf and Milky Way galaxies (§ 3.2), and present results from our full parameter exploration of solutions to the wind equation (§ 3.3). In § 3.4 we derive analytic scaling relations for wind properties, and compare to our numerical integrations. Section 3.5 explores the effects of varying angular momentum and magnetic field strength on wind solutions. The key output of our study is a theoretical prediction for the mass-loss rates and mass-loading factors of cosmic-ray driven disk winds, which we discuss in § 3.6. Finally, § 4 summarizes and discussed our main conclusions. In Appendix A we provide estimates for the effect of ion-neutral collision-induced wave damping on the cosmic ray streaming speed, and in Appendix B we provide additional details related to the behavior of the effective sound speed.

2. ANALYSIS

2.1. *Hydrodynamic Equations*

We begin with the equations governing the combined gas and cosmic ray fluid flow (e.g. Breitschwerdt et al. 1991). The fluid variables are gas density ρ , gas velocity \mathbf{v} , gas pressure P , gas internal energy density \mathcal{E} , magnetic field \mathbf{B} , cosmic ray pressure Π , and cosmic ray energy density \mathcal{E}_{cr} . The Alfvén velocity is given by $\mathbf{v}_A = \mathbf{B}/(4\pi\rho)^{1/2}$, and the total gravitational potential, including both stars and dark matter, is Φ . The collective flow of cosmic rays along the magnetic field is limited by the streaming instability, in which a mean cosmic ray velocity (relative to the gas) exceeding the Alfvén speed leads to resonant excitation of Alfvén waves that then pitch-angle scatter the cosmic rays (Kulsrud & Pearce 1969). We assume that wave damping keeps the amplitude of excited waves low, and also mediates the transfer of momentum from the cosmic ray fluid to the gas (e.g. Kulsrud 2005; Zweibel 2017). Although very efficient wave damping can lead to faster streaming (Everett & Zweibel 2011; Wiener et al. 2013, 2017), we shall assume that the mean velocity of the cosmic ray distribution in the rest frame of the gas is equal to \mathbf{v}_A .¹

We adopt a cylindrical coordinate system with unit vectors \hat{R} , \hat{z} , and $\hat{\phi}$, with $z = 0$ in the midplane of the galactic disk. We take Ω as the local mean rotational velocity of ISM gas in the disk where the wind originates. The inertial-frame velocity \mathbf{v} is related to the velocity \mathbf{u} in a frame rotating with angular velocity $\Omega\hat{z}$ by

$$\mathbf{v} = \mathbf{u} + \Omega R \hat{\phi}. \quad (2)$$

Mass conservation is expressed by

$$\partial_t \rho + \nabla \cdot (\rho \mathbf{v}) = 0. \quad (3)$$

¹ The drift speed v_D of the cosmic ray fluid relative to the gas depends on the damping mechanism for the Alfvén waves responsible for pitch-angle scattering. Wiener et al. (2017) Equations (6) and (7) respectively provide estimates for the streaming speed under assumptions of nonlinear Landau damping and turbulent damping. In both cases, $v_D \sim v_A$ for the parameter regime we consider, consistent with our assumption. Ion-neutral collisions can further damp waves, but for coronal regions where galactic winds originate the neutral density is low and wave damping is weak (see Appendix A).

The momentum equation for the gas in the inertial frame is

$$\partial_t \mathbf{v} + \mathbf{v} \cdot \nabla \mathbf{v} + \frac{\nabla P}{\rho} + \frac{\nabla \Pi}{\rho} = -\nabla \Phi + \frac{(\nabla \times \mathbf{B}) \times \mathbf{B}}{4\pi\rho}, \quad (4)$$

which becomes

$$\partial_t \mathbf{u} + \mathbf{u} \cdot \nabla \mathbf{u} + 2\boldsymbol{\Omega} \times \mathbf{u} + \frac{\nabla(P + \Pi)}{\rho} = -\nabla \left(\Phi - \frac{\Omega^2 R^2}{2} \right) + \frac{(\nabla \times \mathbf{B}) \times \mathbf{B}}{4\pi\rho} \quad (5)$$

in the rotating frame.

Assuming that the cosmic ray fluid streams along the magnetic field at velocity $\mathbf{v} + \mathbf{v}_A$, and that cosmic ray diffusion and radiative and collisional energy losses may be neglected, the energy equation for the cosmic ray fluid is

$$\partial_t \mathcal{E}_{\text{cr}} + \nabla \cdot [(\mathbf{v} + \mathbf{v}_A)(\mathcal{E}_{\text{cr}} + \Pi)] = (\mathbf{v} + \mathbf{v}_A) \cdot \nabla \Pi. \quad (6)$$

Note that $\mathbf{v} \cdot \nabla \Pi$ represents the work done by the cosmic ray fluid in accelerating the gas, and $\mathbf{v}_A \cdot \nabla \Pi$ represents energy losses due to generation of Alfvén waves.

The general form for the internal energy equation for the gas is given by

$$\partial_t \mathcal{E} + \nabla \cdot [\mathbf{v}(\mathcal{E} + P)] = \mathbf{v} \cdot \nabla P - \mathbf{v}_A \cdot \nabla \Pi - \rho \mathcal{L}, \quad (7)$$

where $\rho \mathcal{L}$ is the net radiative loss per volume per time. The term $\mathbf{v} \cdot \nabla P$ represents work done in accelerating the flow, while the term $-\mathbf{v}_A \cdot \nabla \Pi$ represents heat energy gained by wave damping.

For $\mathcal{E}_{\text{cr}} = \Pi/(\gamma_{\text{cr}} - 1)$, $\mathcal{E} = P/(\gamma - 1)$, and an axisymmetric flow, the cosmic ray and gas thermal energy equations become

$$\partial_t \Pi + (\mathbf{u} + \mathbf{v}_A) \cdot \nabla \Pi + \gamma_{\text{cr}} \Pi \nabla \cdot (\mathbf{u} + \mathbf{v}_A) = 0 \quad (8)$$

and

$$\partial_t P + \mathbf{u} \cdot \nabla P + \gamma P \nabla \cdot \mathbf{u} = -(\mathbf{v}_A \cdot \nabla \Pi + \rho \mathcal{L})(\gamma - 1). \quad (9)$$

Previous steady state wind solutions adopt Equations 3, 5, 8, and 9 with $\partial_t = 0$, usually also taking $\mathcal{L} = 0$.

We are interested in winds consisting of warm gas that is maintained at $T \sim 10^4$ K by radiative + shock heating and radiative cooling. Rather than implementing gas heating and cooling terms, for simplicity we instead adopt an isothermal equation of state with $P = \rho c_s^2$ along streamlines for c_s the constant sound speed. This is equivalent to $\gamma = 1$ in Equation 9 because $\nabla \cdot \mathbf{u} = -\mathbf{u} \cdot \nabla \ln \rho$ from the continuity equation.²

We assume that Lorentz forces $(\nabla \times \mathbf{B}) \times \mathbf{B}$ are negligible, so that in axisymmetry the $\hat{\phi}$ component of Equation (5) implies angular momentum is conserved along each streamline,

$$v_\phi R = (u_\phi + \Omega R)R = J = \text{const}. \quad (10)$$

² We note that when $\gamma \neq 1$, for $\mathcal{L} = 0$ the cosmic ray energy equation, gas thermal energy equation, and momentum equation (dotted with $\rho \mathbf{v}$) can be combined to obtain an equation expressing total energy conservation in the flow, $\nabla \cdot \left[\frac{1}{2} v^2 \rho \mathbf{v} + \frac{\gamma}{\gamma-1} P \mathbf{v} + \Phi \rho \mathbf{v} + \frac{\gamma_{\text{cr}}}{\gamma_{\text{cr}}-1} \Pi (\mathbf{v} + \mathbf{v}_A) \right] = 0$, which is related to the Bernoulli equation. While this expression does not apply when $\gamma = 1$, a different Bernoulli-like equation can be obtained in that case (see § 2.5).

With $\mathbf{u}_p = u_R \hat{R} + u_z \hat{z}$ the poloidal velocity, the poloidal components of Equation (5) becomes

$$\mathbf{u}_p \cdot \nabla \mathbf{u}_p + \frac{\nabla(P + \Pi)}{\rho} = -\nabla\Phi + \frac{v_\phi^2}{R} = -\nabla\Psi, \quad (11)$$

where the effective potential

$$\Psi \equiv \Phi + \frac{J^2}{2R^2} \quad (12)$$

incorporates centrifugal-force effects.

2.2. Flow Streamlines and Conserved Quantities

A major assumption in this work is that the poloidal components of the fluid and Alfvén velocities and the gradients of the pressures are all aligned with the gradient of the effective gravitational potential $\nabla\Psi$. We assume that all these vectors lie along \hat{s} , the streamline direction. For streamlines in the poloidal (R-z) plane, the tangent direction is

$$\hat{s} = \frac{(dR/dz)\hat{R} + \hat{z}}{[(dR/dz)^2 + 1]^{1/2}}. \quad (13)$$

The normal to the streamline in the poloidal plane is given by

$$\hat{t} = \frac{\hat{R} - (dR/dz)\hat{z}}{[(dR/dz)^2 + 1]^{1/2}}. \quad (14)$$

Since \hat{s} lies along the gradient of Ψ ,

$$\hat{t} \cdot \nabla\Psi = 0, \quad (15)$$

and the streamline can be found from the potential by solving

$$\frac{dR}{dz} = \frac{\partial\Psi/\partial R}{\partial\Psi/\partial z}. \quad (16)$$

The distance s along the streamline is obtained from

$$\frac{ds}{dz} = \left[1 + \left(\frac{dR}{dz} \right)^2 \right]^{1/2}. \quad (17)$$

The area A of a given fluid element (or the axisymmetric area A between two poloidal streamlines) varies with s as

$$d_s \ln A = \nabla \cdot \hat{s}, \quad (18)$$

where the right-hand side is obtained from applying the divergence to Equation (13) with Equation (16). As an example, radial streamlines have $\hat{s} = \hat{r}$, and $d_r \ln A = \nabla \cdot \hat{r} = 2/r$ so that $A \propto r^2$. If z is taken as the independent variable, we instead have

$$d_z \ln A = \frac{ds}{dz} d_s \ln A, \quad (19)$$

and use Equation (17).

Figure 1 shows examples of streamlines emerging from the disk for a Milky Way potential Φ , for a range of values of J in Ψ . For each footpoint the five values of J correspond to 0, 0.8, 0.9, 0.95, and 1.0 times the respective maximum value on each footpoint. These maximum values correspond to the angular momentum of a circular orbit at radii of 0.59, 1.39, 2.99, 6.74, and 15.14 kpc, respectively, for a halo with virial radius 250 kpc. These values scale with the virial radius. See § 3.1 for details regarding the potential, and § 3.5 for a discussion of J and definition of the maximum value.

Henceforth, we use u to denote the magnitude of the poloidal gas velocity, with

$$\mathbf{u}_p = u\hat{s}, \quad (20)$$

and similarly

$$\mathbf{v}_{A,p} = v_A\hat{s}. \quad (21)$$

From mass conservation (Equation 3), $\nabla \cdot (\rho u\hat{s}) = 0$, which implies $d_s \ln \rho = -(d_s \ln u + d_s \ln A)$. Thus,

$$\rho = \rho_0 \left(\frac{uA}{u_0A_0} \right)^{-1} = \rho_c \left(\frac{uA}{u_cA_c} \right)^{-1} \quad (22)$$

where the “0” subscript denotes values at the streamline footpoint, and the “c” subscript denotes values at the streamline critical point (see § 2.4 for a discussion of critical points).

Similarly, the cosmic ray energy equation (Equation 8) becomes

$$\Pi = \Pi_0 \left(\frac{u + v_A}{u_0 + v_{A,0}} \frac{A}{A_0} \right)^{-\gamma_{\text{cr}}} = \Pi_c \left(\frac{u + v_A}{u_c + v_{A,c}} \frac{A}{A_c} \right)^{-\gamma_{\text{cr}}}; \quad (23)$$

for n_{cr} the cosmic ray number density, this is consistent with conservation of the flow of cosmic ray particles, $(u + v_A)An_{\text{cr}} = \text{const.}$, together with the relation $\Pi \propto n_{\text{cr}}^{\gamma_{\text{cr}}}$.

Since $\nabla \cdot \mathbf{B} = 0$ and $\mathbf{B}_p = B\hat{s}$, $d_s \ln B = -d_s \ln A$ so $B \propto A^{-1}$ and the Alfvén speed $v_A = B/\sqrt{4\pi\rho}$ evolves as

$$v_A = v_{A,0} \left(\frac{u/A}{u_0/A_0} \right)^{1/2} = v_{A,c} \left(\frac{u/A}{u_c/A_c} \right)^{1/2}. \quad (24)$$

This expresses the combined conservation of magnetic flux and mass flux.

Note that the ratio of the Alfvén speed to the wind speed evolves as

$$\begin{aligned} \frac{v_A}{u} &= \frac{v_{A,0}}{u_0} \left(\frac{uA}{u_0A_0} \right)^{-1/2} = \frac{v_{A,0}}{u_0} \left(\frac{\rho}{\rho_0} \right)^{1/2} \\ &= \frac{v_{A,c}}{u_c} \left(\frac{uA}{u_cA_c} \right)^{-1/2} = \frac{v_{A,c}}{u_c} \left(\frac{\rho}{\rho_c} \right)^{1/2}. \end{aligned} \quad (25)$$

For an accelerating wind whose streamlines are opening, both u and A monotonically increase with s while ρ decreases, so v_A/u must decrease with increasing s .

2.3. One-dimensional Steady Wind Equation

Applying the assumptions described in § 2.1 and § 2.2 to Equation 11, the poloidal momentum equation becomes

$$ud_s u + c_s^2 d_s \ln \rho - \gamma_{\text{cr}} \frac{\Pi}{\rho} d_s \ln [(u + v_A)A] = -d_s \Psi. \quad (26)$$

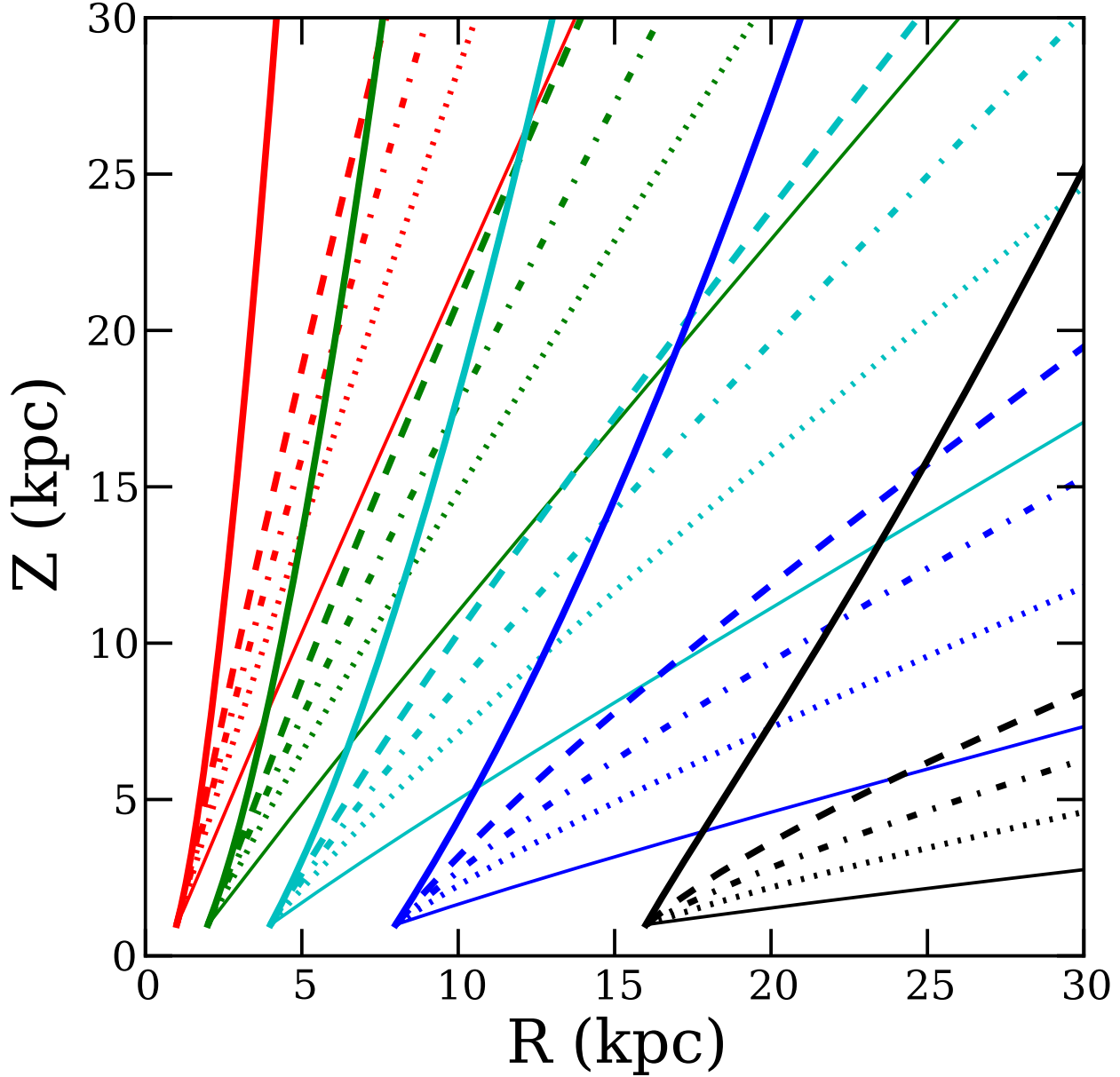


Figure 1. A set of example streamlines starting at $z = 1$ kpc and $R_0 = 2^N$ kiloparsecs. The different line styles correspond to different values of J within a representative Milky Way potential with $V_H = 250$ km s $^{-1}$ and $R_{\text{vir}} = 250$ kpc. A larger value of J provides an outward acceleration which counters some of the inward gravitational acceleration, which causes the streamline to be more vertical. See text for details.

After some manipulation, we find

$$\left(u^2 - c_s^2 - \gamma_{\text{cr}} \frac{\Pi}{\rho} \frac{u + v_A/2}{u + v_A} \right) d_s u = u \left(-d_s \Psi + c_s^2 d_s \ln A + \gamma_{\text{cr}} \frac{\Pi}{\rho} \frac{u + v_A/2}{u + v_A} d_s \ln A \right). \quad (27)$$

We define an effective sound speed C_{eff} , including effects of both gas and cosmic ray pressure, by the expression

$$C_{\text{eff}}^2 \equiv c_s^2 + \gamma_{\text{cr}} \frac{\Pi}{\rho} \frac{u + v_A/2}{u + v_A} \quad (28)$$

(cf. Equations 30 and 31 of [Ipavich 1975](#)).

Starting from [Equation 23](#) and using [Equation 22](#) and [Equation 25](#), one can show that

$$\frac{d\Pi}{d\rho} = \gamma_{\text{cr}} \frac{\Pi}{\rho} \frac{u + v_A/2}{u + v_A}. \quad (29)$$

Thus, C_{eff}^2 in [Equation 28](#) can also be written as

$$C_{\text{eff}}^2 = \frac{dP}{d\rho} + \frac{d\Pi}{d\rho}. \quad (30)$$

We define a gravitational velocity V_g by the expression

$$V_g^2 \equiv \frac{d_s \Psi}{d_s \ln A}. \quad (31)$$

We note that if streamlines are radial and the centrifugal term in Ψ is negligible, $V_g^2 = r d_r \Phi / 2 = v_c^2(r)/2$ for $v_c(r)$ the circular velocity at distance r . Thus, if the circular velocity is a nearly constant value characterized by the galaxy's dark matter halo, $V_g \sim V_H/\sqrt{2}$.

With the above definitions, the ordinary differential equation that describes the steady-state wind is given by

$$d_s u = u \frac{(V_g^2 - C_{\text{eff}}^2)}{(C_{\text{eff}}^2 - u^2)} d_s \ln A \quad (32)$$

Written in this way, the wind equation ([Equation 32](#)) has the same form as that of a classical Parker wind in a Keplerian potential, taking $s \rightarrow r$, $C_{\text{eff}}^2 \rightarrow dP/d\rho \equiv c_s^2$, $V_g^2 \rightarrow (1/2)GM/r$, and $d_s \ln A \rightarrow 2/r$. In the case of general rather than radial streamlines, it is convenient to use z rather than s as the independent variable, in which case the wind equation may be written

$$d_z u = u \frac{(V_g^2 - C_{\text{eff}}^2)}{(C_{\text{eff}}^2 - u^2)} d_z \ln A. \quad (33)$$

We note that the density ρ (or gas pressure ρc_s^2) appears in the wind equation only in ratios with the magnetic pressure (in v_A) and the cosmic ray pressure. For integration of the wind equation, we therefore only require the combination

$$\begin{aligned} \frac{\Pi}{\rho} &= \frac{\Pi_0}{\rho_0} \left(\frac{u + v_A}{u_0 + v_{A,0}} \frac{A}{A_0} \right)^{-\gamma_{\text{cr}}} \left(\frac{uA}{u_0 A_0} \right) \\ &= \frac{\Pi_c}{\rho_c} \left(\frac{u + v_A}{u_c + v_{A,c}} \frac{A}{A_c} \right)^{-\gamma_{\text{cr}}} \left(\frac{uA}{u_c A_c} \right) \end{aligned} \quad (34)$$

rather than [Equation 22](#) and [Equation 23](#) separately.

To obtain wind solutions, we evolve u , A , and the streamline using [Equation 33](#), [Equation 19](#), and [Equation 16](#) as a set of three coupled ordinary differential equations. For any point on the streamline where we have u and A , we find v_A and Π/ρ in terms of u and A via [Equation 24](#) and [Equation 34](#), respectively.

2.4. Critical Point and Integration Method

A physically realistic wind begins close to the galactic disk from a velocity u that is low compared to the effective sound speed C_{eff} and the gravitational speed V_g . From Equation 32, for an accelerating wind with $d_s u > 0$, it must be true that $V_g > C_{\text{eff}}$ for $u < C_{\text{eff}}$, and $V_g < C_{\text{eff}}$ for $u > C_{\text{eff}}$. If the fluid is to achieve speeds that will allow it to escape into the galaxy's halo, u must exceed both C_{eff} and V_g . Since $d_s \ln A$ is set by the shape of the potential Ψ , it is in general non-zero. Thus, for the flow to avoid singularities (i.e. $d_s u$ is never infinite), at the critical point where $u = C_{\text{eff}}$ it must also be true that $V_g = C_{\text{eff}}$.

From Equation 28, one can show (see Appendix B) that

$$\text{sgn}(d_s C_{\text{eff}}^2) = \text{sgn}(d_s \rho) \text{sgn} \left[\gamma_{\text{cr}} \left(1 + \frac{1}{2} \frac{v_A}{u} \right)^2 - 1 - \frac{7}{4} \frac{v_A}{u} - \frac{1}{2} \frac{v_A^2}{u^2} \right]. \quad (35)$$

For $\gamma_{\text{cr}} = 4/3$, C_{eff} will increase outward (as ρ decreases) whenever $v_A/u > 0.64$. From Equation 25, v_A/u is strictly decreasing with s if ρ is decreasing, so provided that $v_A/u > 0.64$ at the critical point, C_{eff} will secularly increase from the footpoint up to the critical point. A schematic showing u , C_{eff} , and V_g relative to one another as a function of streamline distance, including a critical transition, is shown in Figure 2.³

For a given galactic potential and streamline shape, the location of the critical transition $R = R_c$, $z = Z_c$ fully specifies the value of $V_{g,c}$. Thus, a given location for the critical point also specifies the fluid velocity u_c and value of $C_{\text{eff},c}$ at that point.

We obtain wind solutions to our set of ODEs with the following procedure: Given some desired footpoint (R_0, Z_0) in the effective potential, we pre-compute the streamline which passes through that footpoint by integrating Equation 16 outward. Then, one may choose some point (R_c, Z_c) along that streamline to be the critical point; this also specifies the values of $V_{g,c} = u_c = C_{\text{eff},c}$ and A_c based on the potential and streamline shape at the critical point. Given (R_c, Z_c) , one may select a value of the Alfvén speed at the critical point, $v_{A,c}$. Then, applying Equation 28 at the critical point yields Π_c/ρ_c in terms of $V_{g,c}$, $v_{A,c}$, and c_s . With all the fluid variables known at the critical point, the coupled ODEs may be integrated back to the footpoint (R_0, Z_0) according to the procedure described at the end of § 2.3. When the streamline footpoint is reached, the starting “ISM conditions” u_0 , $v_{A,0}$, and Π_0/ρ_0 that are consistent with the selected critical point are read off of the solution.

For each footpoint, a variety of solutions can be attained by (1) varying the critical point location (R_c, Z_c) along the streamline, and (2) varying the Alfvén velocity at the critical point, $v_{A,c}$. In total, this implies two degrees of freedom for each footpoint and streamline shape. Equivalently, two degrees of freedom also represents choosing the footpoint values of Π_0/ρ_0 and $v_{A,0}^2 = B_0^2/(4\pi\rho_0)$, with u_0 the unique value for which a solution is able to pass through a critical point. Thus, we can explore a range of ISM properties given a footpoint, and can use 2-D root-finding to locate wind solutions (including the value u_0) of particular points in Π_0/ρ_0 and $B_0^2/(4\pi\rho_0)$ space, while using the critical point location and $v_{A,c}$ as inputs. More generally, any two of the three footpoint velocities $(\Pi_0/\rho_0)^{1/2}$, $v_{A,0}$, u_0 can be chosen to parameterize the space of possible solutions, with the third velocity constrained by the requirement that the flow makes a critical transition.

³ We discuss in § 3.4 the key differences between a Parker-type stellar winds driven by thermal pressure in a point mass potential, versus galactic winds driven by cosmic ray pressure in an extended dark matter halo potential.

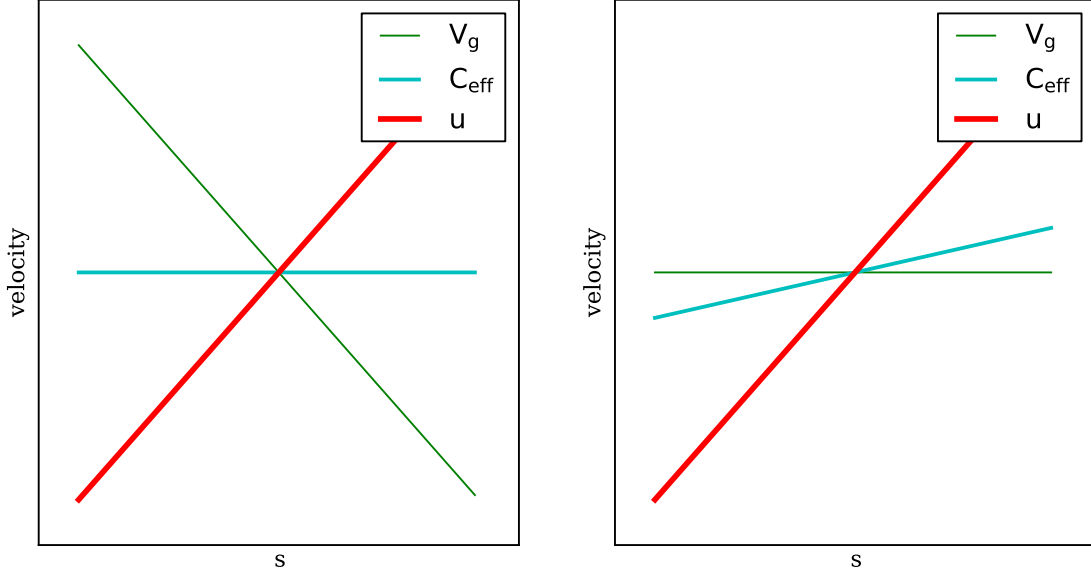


Figure 2. A schematic comparing the behavior near the critical point of an isothermal Parker wind in a Keplerian potential (left) to that of a wind driven by cosmic ray pressure in a galactic potential (right). Loci depicting the gravitational velocity V_g , effective sound speed C_{eff} , and wind velocity u as a function of distance along the streamline s are shown. Note that all three curves intersect at the critical point (or sonic point). Also note that in each case, $u < C_{\text{eff}} < V_g$ at low s , and $V_g < C_{\text{eff}} < u$ at high s , consistent with the wind equation (Equation 32) for an accelerating flow. For the schematic Parker wind depicted, C_{eff} is constant (isothermal) and V_g is decreasing (Keplerian). For the schematic cosmic ray driven wind, V_g is nearly constant (galactic potentials have close to flat rotation curves), which necessitates an increasing C_{eff} to enable a critical transition. More generally, if $P_e \propto \rho^{\gamma_e}$, $C_{\text{eff}}^2 \equiv dP_e/d\rho \propto \rho^{\gamma_e-1}$, so a critical transition is only possible in $V_g \sim \text{const}$ galactic potentials if $\gamma_e < 1$, whereas critical transitions are possible in Keplerian potentials ($V_g \propto r^{-1/2}$) for $\gamma_e \geq 1$.

To initiate integration near the critical point, we apply L'Hôpital's rule to the right-hand side of Equation 32:

$$\begin{aligned}
 d_s u &= \lim_{s \rightarrow s_c} u \frac{(V_g^2 - C_{\text{eff}}^2)}{(C_{\text{eff}}^2 - u^2)} d_s \ln A = u_c d_s \ln A \frac{\frac{d}{ds} (V_g^2 - C_{\text{eff}}^2)}{\frac{d}{ds} (C_{\text{eff}}^2 - u^2)} \\
 &= u_c d_s \ln A \frac{[d_s V_g - (\partial_A C_{\text{eff}} d_s A + \partial_u C_{\text{eff}} d_s u)]}{[\partial_A C_{\text{eff}} d_s A + \partial_u C_{\text{eff}} d_s u - d_s u]},
 \end{aligned} \tag{36}$$

where we use $u_c = V_{g,c} = C_{\text{eff},c}$ at the critical point and the partial derivatives with respect to u assume holding A constant and vice versa. Note that C_{eff} can be written as a function of u and A .

This yields a quadratic which must be solved for $d_s u$, after computing $\partial_A C_{\text{eff}}$, $\partial_u C_{\text{eff}}$, $d_s A$, and $d_s V_g$ (see Appendix B). The two possible solutions are a decelerating wind and accelerating wind, and the accelerating solution is taken. Alternatively, using the properties of the solution topology, different values of $f(u, s) = d_s u$ can be tested. Each value of $d_s u$ will result in some $u' = u_c - d_s u \Delta s$ for a new point $s' = s_c - \Delta s$. Then, taking this value of u' and position on the streamline $s' = s_c - \Delta s$, the derivative $f(u', s')$ can be calculated. The true $f(u, s) = d_s u$ will be a fixed point such that

$f(u, s) = f(u', s') = f(u - f(u, s)\Delta s, s - \Delta s)$ and can be numerically found. This only holds true for the true wind solution passing through the critical transition, and does not hold true for the breeze solutions, due to the solution topology of wind flows. Any error in this technique is comparable to a shooting technique error, as even an order unity error in $d_s u$ leads to a point within $\Delta s d_s u$ of the critical point. That is, we begin near the sonic point in (s, u) space, as long as the initial step Δs is chosen to be small, which avoids the sensitive nature of $d_s u$ near the sonic point and gives us an accurate wind. Integration can proceed directly from there.

2.5. Bernoulli Equation

From Equation 22, Equation 31, and Equation 32 it is straightforward to show that

$$d_s \left(\frac{1}{2} u^2 + \Psi \right) = -C_{\text{eff}}^2 d_s \ln \rho. \quad (37)$$

With Equation 30, Equation 37 then becomes

$$d_s \left(\frac{1}{2} u^2 + \Psi \right) = - \left(\frac{d_s P}{\rho} + \frac{d_s \Pi}{\rho} \right). \quad (38)$$

For an isothermal equation of state for the gas, $dh_g = dP/\rho$ for gas enthalpy $h_g = c_s^2 \ln \rho$. We can formally define cosmic ray enthalpy h_{cr} via $dh_{\text{cr}} = d\Pi/\rho$. With this definition we have

$$d_s \left(\frac{1}{2} u^2 + \Psi + h_g + h_{\text{cr}} \right) \equiv d_s \mathcal{B} = 0 \quad (39)$$

for Bernoulli parameter \mathcal{B} . In general, Equation 29 does not yield a simple analytic form for h_{cr} . However, in the limit of either $u \gg v_A$ or $u \ll v_A$ we have $\Pi \propto \rho^{\gamma_{\text{cr}}}$ or $\Pi \propto \rho^{\gamma_{\text{cr}}/2}$, respectively, such that

$$h_{\text{cr}} \rightarrow \begin{cases} \frac{\gamma_{\text{cr}}}{\gamma_{\text{cr}}-1} \frac{\Pi}{\rho} & \text{for } u \gg v_A \\ \frac{\gamma_{\text{cr}}}{\gamma_{\text{cr}}-2} \frac{\Pi}{\rho} & \text{for } u \ll v_A \end{cases} \quad (40)$$

in the two limiting cases.

With $\gamma_{\text{cr}} = 4/3$, $h_{\text{cr}} \rightarrow 4(\rho/\rho_0)^{1/3} \Pi_0/\rho_0$ and $C_{\text{eff}}^2 \rightarrow (4/3)(\rho/\rho_0)^{1/3} \Pi_0/\rho_0$ for $u \gg v_A$, while $h_{\text{cr}} \rightarrow -2(\rho/\rho_0)^{-1/3} \Pi_0/\rho_0$ and $C_{\text{eff}}^2 \rightarrow (2/3)(\rho/\rho_0)^{-1/3} \Pi_0/\rho_0$ for $u \ll v_A$. The case $u \gg v_A$ has the same characteristic behavior as gas enthalpy, in that h_{cr} is positive and both h_{cr} and C_{eff} decrease in magnitude as ρ decreases. The limit $u \ll v_A$, which is more relevant for understanding wind solutions inside the critical point, has instead very different behavior: h_{cr} is negative, and both h_{cr} and C_{eff} increase in magnitude as ρ decreases. It is this behavior for h_{cr} and C_{eff} that allows u to increase and smoothly pass through a critical point where $u = V_g = C_{\text{eff}}$ even when V_g is nearly flat in s (see Figure 2).

3. RESULTS

3.1. Model Specification

Our goal is to explore the dependence of possible wind properties, and especially mass-loss rates, on the galactic environment. Winds will be affected by both the properties of the ISM in which the wind originates, and the galactic potential in which it is accelerated.

To represent a range of galactic potentials, we adopt the general form of [Bovy \(2015\)](#) for the Milky Way potential. This includes a power law bulge, a Miyamoto-Nagai disk, and an NFW dark matter halo. To allow for a range of galaxy masses and sizes, we also wish to consider potentials with varying virial radius R_{vir} and virial velocity V_H . To do this, we consider a family of Milky-Way-like potentials in which the mean density is the same, but mass and virial velocity of the NFW halo vary with halo virial radius R_{vir} according to $M_H \propto R_{\text{vir}}^3$ and $V_H^2 \propto GM_H/R_{\text{vir}} \propto R_{\text{vir}}^2$, with $V_H/\text{km s}^{-1} = R_{\text{vir}}/\text{kpc}$. The disk and bulge mass and size are rescaled in the same way.

Within a given potential, we sample a few different footpoint locations, and for each footpoint, we consider a range of the angular momentum J (see [Figure 1](#) and detailed parameter discussion in [§ 3.3](#)). Each footpoint location R_0 and choice of angular momentum $J/(\Omega R_0^2)$ defines a streamline. For each streamline, we explore a two-dimensional parameter space of the sonic point location z_c/R_{vir} and Alfvén speed at the critical point $v_{A,c}$. As discussed in [§ 2.4](#), this two-dimensional parameter space maps to a two-dimensional parameter space of footpoint initial conditions for the wind at a distance $z = 1$ kpc above the disk midplane.

The ISM in the coronal region may have a range of gas, magnetic, and cosmic ray pressures. These depend on the midplane ISM properties as well as the star formation activity, which drives a galactic fountain that circulates gas from the midplane to coronal regions. We non-dimensionalize the problem so that the three relevant pressures are captured as two ratios: the thermal gas pressure to cosmic ray pressure ratio $P_0/\Pi_0 = c_s^2(\Pi_0/\rho_0)^{-1}$, and the magnetic field pressure to cosmic ray pressure ratio $B_0^2/(8\pi\Pi_0) = (1/2)v_{A,0}^2(\Pi_0/\rho_0)^{-1}$. We note that $v_{A,0}^2$ and Π_0/ρ_0 are obtained from outputs of the wind integration starting at the critical point and ending at the footpoint. We also non-dimensionalize all of the velocities as ratios with respect to c_s , which we set to be 10 km/s for a “cool” wind consisting of warm-phase ISM gas.

We are interested in cases where the magnetic-to-cosmic ray pressure ratio brackets equipartition by an order of magnitude (above and below). Since this ratio is close to equipartition in the Solar neighborhood, and the scale heights of these components are large, we expect that at $z = 1$ kpc they remain roughly in equipartition.

3.2. Sample Wind Solutions

Examples of wind solutions for a dwarf galaxy halo with $V_H = 50 \text{ km s}^{-1}$ and a Milky Way-like halo with $V_H = 250 \text{ km s}^{-1}$ are shown in [Figure 3](#) and [Figure 4](#). For each halo potential, cases with initial launch velocity $u_0 = 5 \text{ km s}^{-1}$ and $u_0 = 50 \text{ km s}^{-1}$ are shown. In all cases, the footpoint cosmic ray pressure and magnetic pressure are chosen to be in equipartition. For the dwarf model, the footpoint radius is $R_0 = 1 \text{ kpc}$, while for the Milky Way model the footpoint radius is $R_0 = 4 \text{ kpc}$. The angular momentum parameter is set to $J = 0$. Specification of u_0 and $B_0^2/(8\pi\Pi_0)$ selects a unique wind solution for a given halo potential and streamline.

For all solutions shown, u secularly increases with distance, while V_g secularly decreases. C_{eff} increases outward inside the critical point, and then decreases at large distance. The Alfvén speed v_A exceeds u inside the critical point, but drops off to small values at large distance. The density ρ and cosmic ray pressure Π secularly decrease with distance. In detail, u becomes nearly constant at large distance, which for a radial flow implies that $\rho \propto (uA)^{-1} \propto r^{-2}$. Thus, from [Equation 25](#), $v_A \propto u\rho^{1/2} \propto r^{-1}$ at large distance, which in turn implies that the effective sound speed declines slowly, as $C_{\text{eff}} \propto \rho^{(\gamma_{\text{cr}}-1)/2} \propto \rho^{1/6} \propto r^{-1/3}$, at large distance (modulo flattening due to c_s). Since both V_g and C_{eff} are equal at the sonic point and decrease slowly thereafter, they tend to be similar up

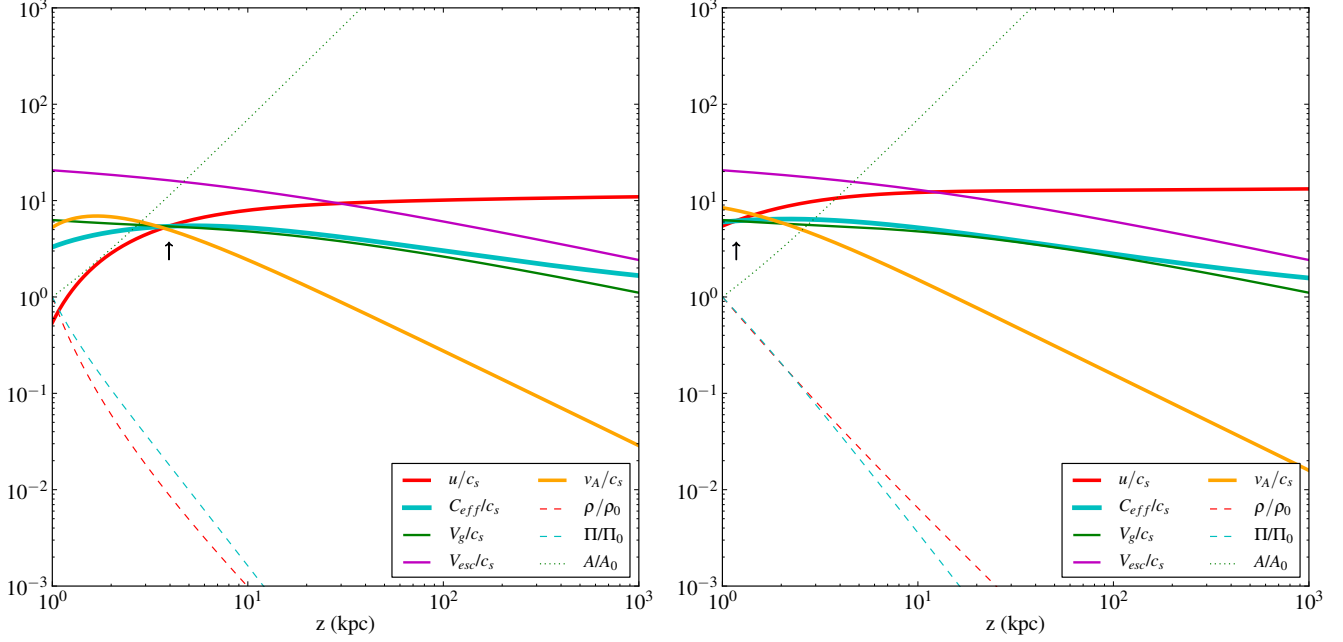


Figure 3. An example solution of the wind equation in a dwarf galaxy potential with $V_H = 50$ km/s, launched at $R = 1$ kpc and $z = 1$ kpc with no angular momentum. For the left and right panels, the wind is launched with initial velocity $u_0 = 5$ km s $^{-1}$ and $u_0 = 50$ km s $^{-1}$, respectively. In both panels, the footpoint cosmic ray and magnetic pressures are chosen to be equal, $B_0^2/(8\pi\Pi_0) = 1$. The black arrow indicates the critical point where $u = V_g = C_{\text{eff}}$, equal to 54 km s $^{-1}$ and 61 km s $^{-1}$ for left and right panels.

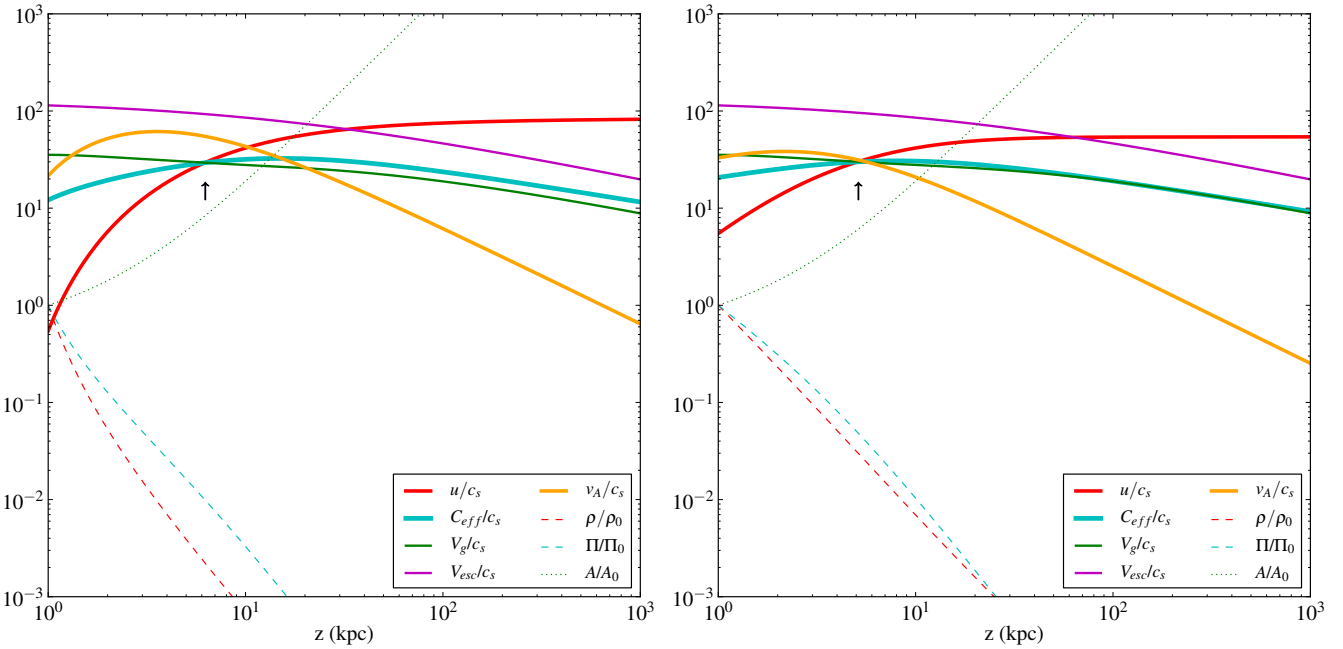


Figure 4. A sample wind solution as in Figure 3, except for a Milky Way potential with $V_H = 250$ km/s, and launched at $R = 4$ kpc. At the critical point, $V_{g,c} = 290, 300$ km s $^{-1}$ for left and right panels, respectively.

until large distance where $C_{\text{eff}} \sim c_s$. The escape speed $V_{\text{esc}} \equiv \sqrt{-2(\Psi - \Psi_\infty)}$ is larger than V_H but decreases with distance, so that u eventually exceeds V_{esc} and in the absence of intervening halo gas, the wind would escape. In practice, wind propagation at large distance would ultimately be limited by interaction with surrounding halo gas.

3.3. Wind Parameter Exploration

We have extensively explored the parameter space of galaxies' potentials and footpoint ISM properties. In particular, we have considered potentials with V_H in the range $50 - 300 \text{ km s}^{-1}$. Our standard set of footpoint locations is $R_0 = 1, 2, 4, 8, 16 \text{ kpc}$, and we vary the angular momentum parameter J by selecting values up to a maximum value for each footpoint, described in § 3.5.

To explore a range of footpoint ISM conditions for each potential and each streamline, in practice we begin by sampling a grid of critical point locations and Alfvén speeds. Some of these points yield footpoint solutions that fall within a few orders of magnitude of equipartition between gas, magnetic field, and cosmic ray pressure. Interpolating between those points yields estimates for values of the critical point location and Alfvén speed whose corresponding winds begin near desired points in the space of footpoint pressure ratios. This allows us to fill in the pressure space even though integration begins from the critical point.

Every computation yields either a wind accelerating through the sonic point or fails immediately by decelerating through the sonic point, which helps to delimit the boundaries of the space in which interesting wind solutions exist. Here, we focus on wind solutions in which u secularly increases with distance. Since accelerating winds require $C_{\text{eff},0} < V_{g,0}$, a lower limit to $\rho_0 c_s^2 / \Pi_0$ is set by conditions that yield $C_{\text{eff},0} = V_g \sim V_H$. If ρ_0 / Π_0 is too low, $C_{\text{eff},0}$ exceeds $V_{g,0}$, and the wind does not accelerate. This lower limit is roughly illustrated by the black dashed horizontal line denoting $\Pi_0 / \rho_0 = (V_H^2 - c_s^2)$ in the upper-left panels of Figure 5 and Figure 6.

When $v_{A,c}/u_c$ is small, C_{eff} is decreasing through the critical point (see Equation 35). Since V_g must decrease faster than C_{eff} for a critical transition to exist, small $v_{A,c}$ ends up producing a sonic point at a large distance. But to yield a sonic point at large distance, $C_{\text{eff},0}$ must be large, and this implies small $\rho_0 c_s^2 / \Pi_0$. Thus, as we are not interested in solutions with sonic points at extremely large distance, this places another lower limit on $\rho_0 c_s^2 / \Pi_0$. For example, the lower left sector of Figure 6 is excluded by these considerations, as can be seen by the large values of z_c and the small values of $v_{A,c}$.

Winds with large $v_{A,c}$ tend to have strong acceleration, implying lower u_0 to reach a given $V_{g,c} \sim V_H$. Although solutions to the wind equation exist for large $v_{A,c}$, we limit $v_{A,c}$ to avoid unrealistically small u_0 . This consideration excludes the upper right sector of Figure 6.

For each wind solution, we are particularly interested in the mass-loss rate. Other parameters of interest are the critical point location and Alfvén speed. In addition, to decide whether a given cosmic-ray driven wind solution can be realistically produced, it is important to consider the footpoint velocity u_0 . Supernova-driven fountains can transfer warm ISM gas from the midplane to the corona, but the velocity of “fountain” gas at $z \gtrsim \text{kpc}$ distances above the midplane is typically $\lesssim 100 \text{ km s}^{-1}$.⁴ A cosmic-ray driven wind must be able to match its footpoint conditions to the

⁴ In particular, from self-consistent ISM/star formation/supernova feedback simulations, Kim & Ostriker (2017, submitted) found that the mass of fountain gas (for Solar neighborhood conditions) exponentially decreases with velocity, with typical outflowing velocity $\sim 50 \text{ km s}^{-1}$ at $z \sim 1 - 3 \text{ kpc}$.

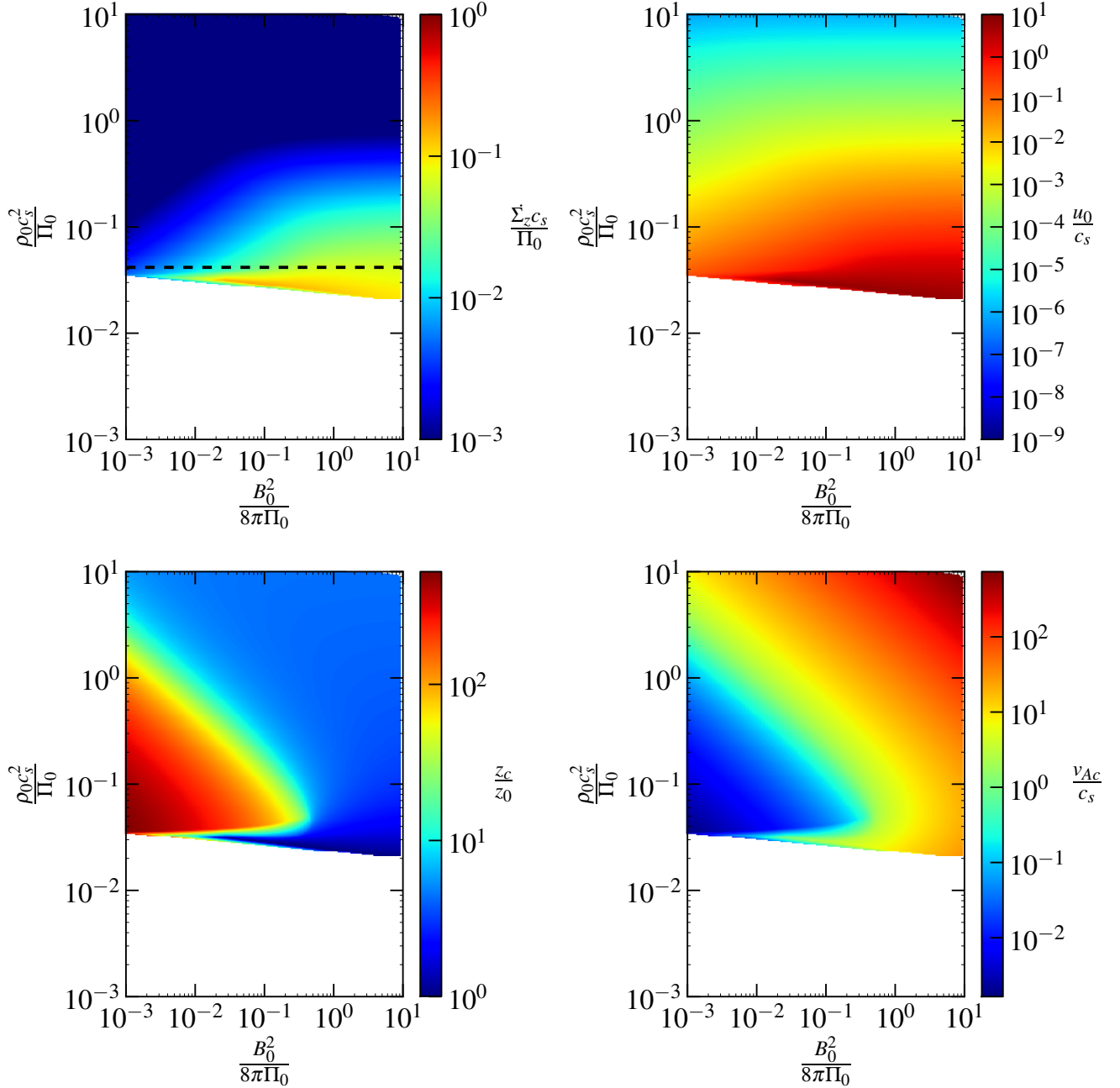


Figure 5. A two-dimensional parameter exploration of solutions of the wind equation in a dwarf galaxy potential with $V_H = 50$ km/s. Results are shown for solutions on streamlines launched at $R = 1.0$ kpc and $z = 1.0$ kpc with no angular momentum. A characteristic wind solution belonging to this set is shown in Figure 3. The top left panel shows in color scale results for the (dimensionless) mass-loss rate per unit area from the disk, $\dot{\Sigma}_z c_s / \Pi_0$, as a function of thermal-to-cosmic-ray and magnetic-to-cosmic-ray pressure ratio at the streamline footpoint. The dashed horizontal line is where $\Pi_0 / \rho_0 = (V_H^2 - c_s^2)$. The top right panel shows the solution for u_0 , the speed of the flow at the footpoint. Bottom left and bottom right panels show solutions for the z location and Alfvén speed at the critical point.

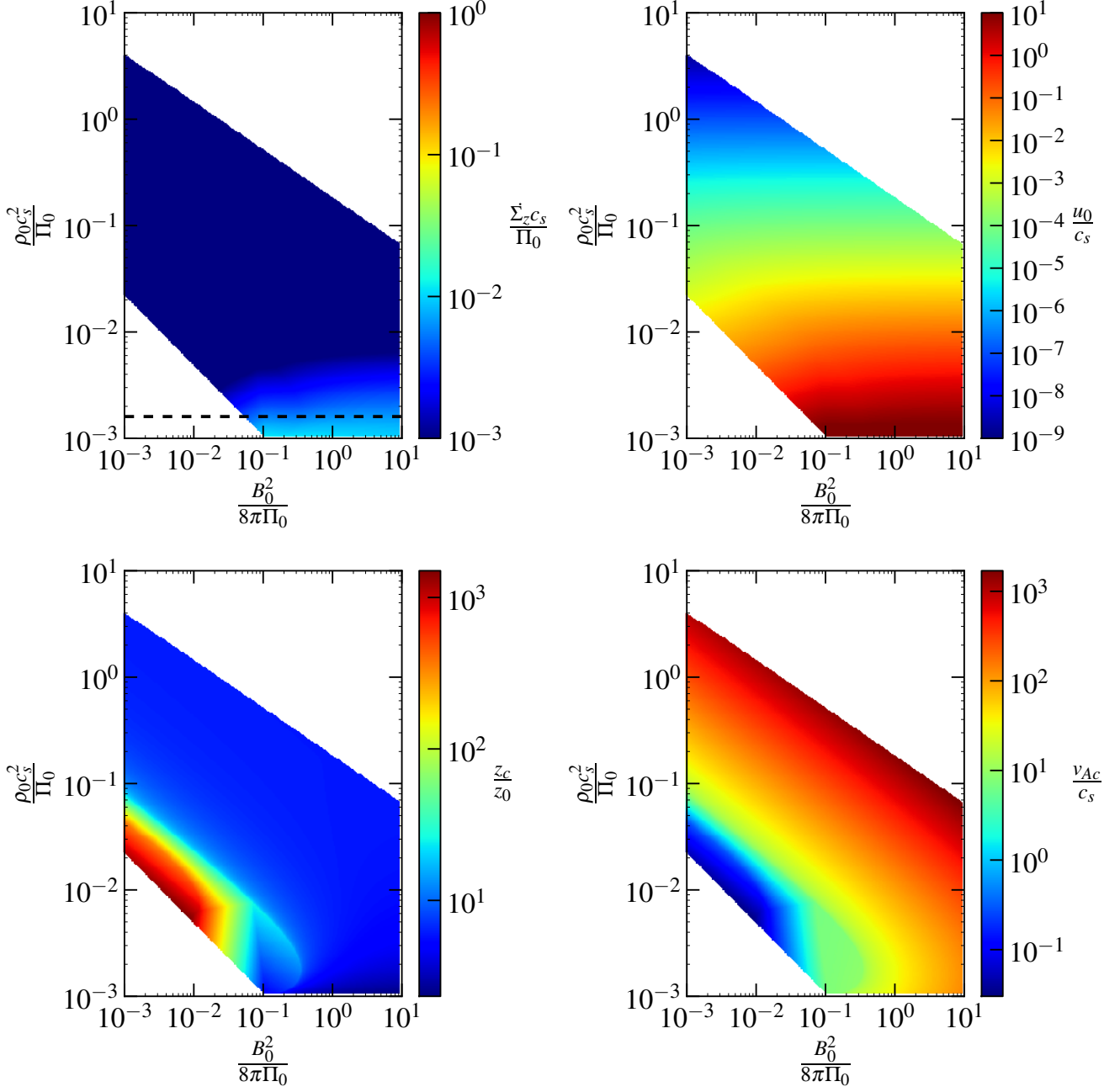


Figure 6. Same as Figure 5, except for a Milky Way-like galaxy potential with $V_H = 250$ km/s, launched at $R = 4$ kpc. A characteristic wind solution belonging to this set is shown in Figure 4.

available gas mass and momentum flux into the corona from below, which implies an upper limit on the value of u_0 .

In characterizing the mass loss produced in our wind solutions, we non-dimensionalize the mass flux by taking the ratio at the footpoint to Π_0/c_s . Considering only the z component of the wind

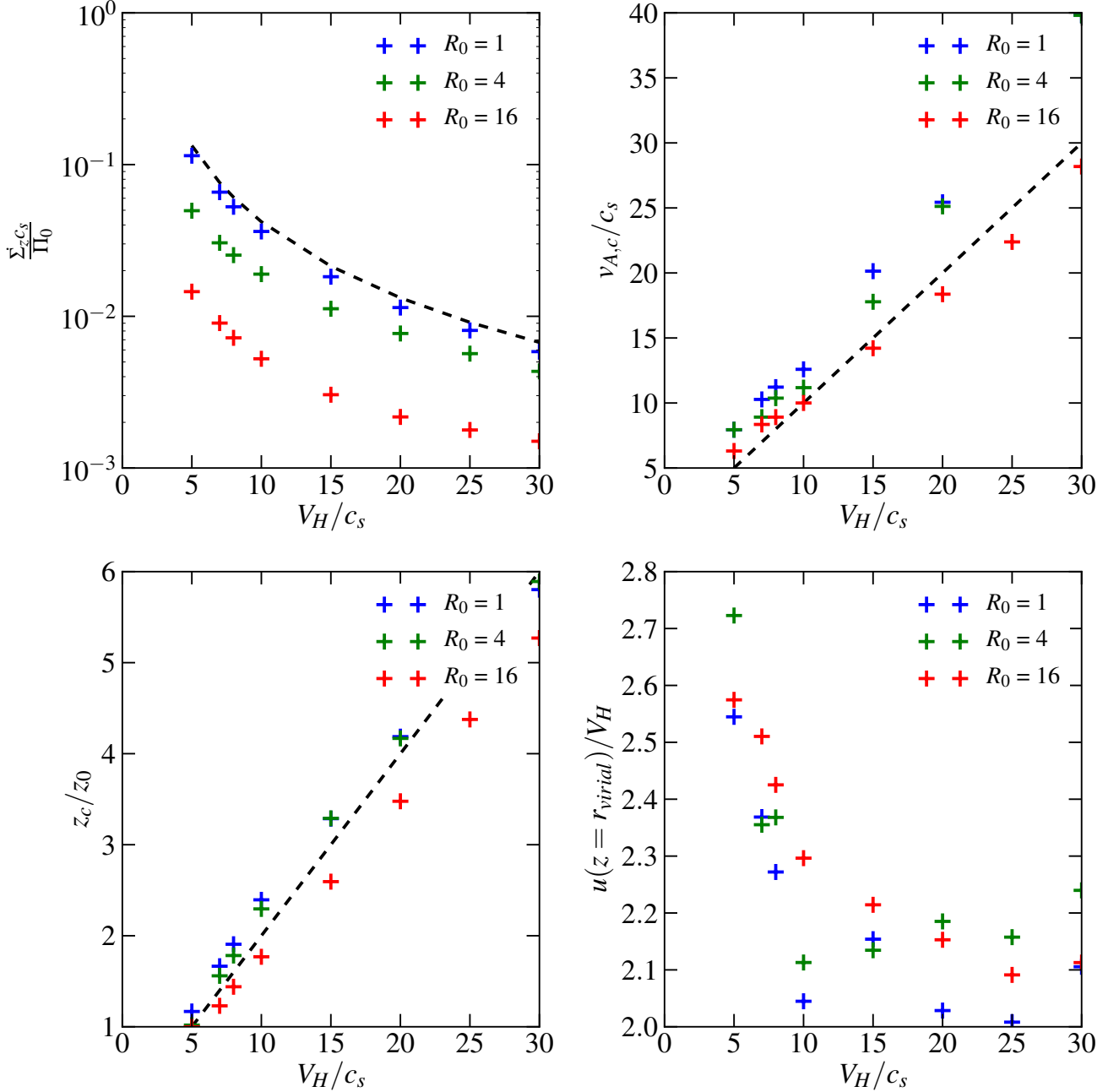


Figure 7. Results from wind solutions for a range of halo velocities V_H and footpoint radii R_0 . For all cases, $\Pi_0 = B_0^2/8\pi$ and $u_0 = 50 \text{ km s}^{-1}$ at the footpoint at height $z_0 = 1 \text{ kpc}$, and $J = 0$. The top left panel shows that at constant u_0 , the mass loss rate decreases with increasing V_H , and that footpoints originating at larger radii have lower (scaled) mass-loss rates. The $\dot{\Sigma}_z$ results are comparable to $\dot{\Sigma}$ from Equation 46 setting $A_c/A_0 = 1$ (dashed black curve), with reduction at larger R_0 in part due to lower $\hat{s} \cdot \hat{z}$. The top right panel shows that the sonic Alfvén speed $v_{A,c}$ scales approximately linearly with V_H (dashed black line represents $v_{A,c} = V_H$), and is slightly larger for smaller R_0 . The bottom left panel shows that the location of the critical point is typically not far from the launch point for winds with near-equipartition cosmic ray and magnetic pressure, with $z_c \propto V_H \propto R_H$ (dashed line). Sonic points in more massive halos are further out because the wind must accelerate more to reach $u = V_g$. The bottom right panel shows that by the time the wind reaches the virial radius, it would reach a speed a few times greater than V_H .

velocity to get the mass loss per unit area of the galactic disk, we have

$$\frac{\dot{\Sigma}_z c_s}{\Pi_0} = \frac{\rho_0 u_{0,z} c_s}{\Pi_0} = \frac{\rho_0 c_s^2}{\Pi_0} \frac{u_{0,z}}{c_s}. \quad (41)$$

Thus, for a given ratio of gas-to-cosmic-ray pressure at the footpoint, the normalized mass flux is set by the normalized vertical component of the footpoint velocity, $u_{0,z}/c_s$.

Examples showing the space of two dimensional pressure ratios for which wind solutions have been found (on a given streamline in a given potential) are shown in [Figure 5](#) and [Figure 6](#). For each point in the identified wind solution space, values of the mass-loss rate, the footpoint velocity, the vertical distance to the critical point, and the Alfvén speed at the critical point are shown in color scale in separate panels.

From the top two panels in [Figure 5](#) and [Figure 6](#), the mass loss rate and initial wind velocity appear to be primarily a function of the gas density with very little dependence on the strength of the magnetic field, when magnetic and cosmic ray pressures are within an order of magnitude of equipartition. Furthermore, comparing winds from massive galaxies (large V_H) to dwarf galaxies shows that increasing V_H shifts the solution space towards lower density (lower $\rho_0 c_s^2/\Pi_0$), and also leads to lower scaled mass loss (lower $\dot{\Sigma}_z c_s/\Pi_0$). This is not qualitatively surprising, as the potential well is deeper (larger $V_g \sim V_H$) in a more massive galaxy, and therefore larger C_{eff} is needed to drive outflows to reach escape speed. Since $C_{\text{eff}}^2 \sim \Pi/\rho$, the mean density of winds in more massive galaxies must be lower if they are to successfully escape. In § 3.4, we demonstrate analytically and numerically that a relationship is expected between mass-loss rate and the ratio $\rho_0 c_s^2/\Pi_0$. Then, from the definition of our dimensionless mass loss rate, a relationship between the gas density and the mass loss rate also fixes the initial wind velocity.

Naively, it might seem surprising that there is a lower bound on the density (or an upper bound on the cosmic ray pressure) for which wind solutions exist in dwarf galaxies. However, the reason for this lower limit is that we are only interested in accelerating winds with low initial velocity. This requires $C_{\text{eff},0} < V_{g,0}$ at the footpoint, as discussed in § 2.4. Since $C_{\text{eff}}^2 \sim \Pi/\rho$, there is an upper limit on what $C_{\text{eff},0}^2$ (and hence the cosmic ray pressure) can be that is still consistent with a given (low) value of $V_g \sim V_H$. Lower density winds with higher $C_{\text{eff},0}$ that are already escaping with $u_0 > C_{\text{eff},0} > V_{g,0}$ are mathematically allowed. However, these are not of interest for the present work, because they are not driven by cosmic ray pressure gradients above the main body of the ISM.

Some general characteristics of winds are illustrated in [Figure 7](#). In this figure, we consider a range of halo velocities ($V_H = 50 - 300 \text{ km s}^{-1}$) and footpoint radii ($R_0 = 1, 4, 16 \text{ kpc}$). We show results of solutions for which the footpoint magnetic field is in equipartition with the cosmic ray pressure ($B_0^2/(8\pi) = \Pi_0$) and the footpoint launch speed is $u_0 = 50 \text{ km s}^{-1}$, with angular momentum $J = 0$ and footpoint height $z_0 = 1 \text{ kpc}$. For each wind solution, we show the scaled mass-loss rate ($\dot{\Sigma}_z c_s/\Pi_0$, [Equation 41](#)), the Alfvén speed at the critical point ($v_{A,c}/c_s$), the vertical distance of the critical point from the footpoint (z_c/z_0), and the flow velocity at large distance relative to the halo velocity ($u[z = R_{\text{vir}}]/v_H$). As might be expected, $v_{A,c}$ and the wind velocity at the virial radius are roughly proportional to V_H , and z_c increases roughly linearly with R_{vir} . The critical point is relatively near the launch point when $B_0^2/(8\pi) = \Pi_0$, as is also evident in [Figure 5](#) and [Figure 6](#). For a given V_H , $\dot{\Sigma}_z c_s/\Pi_0$ is larger for smaller footpoint radius R_0 , and the differential effect is largest at small V_H . The dependence of $\dot{\Sigma}_z c_s/\Pi_0$ on R_0 is largely because streamlines are most vertical for small

R_0 . The scaled mass-loss rate $\dot{\Sigma}_z c_s / \Pi_0$ decreases with V_H ; we discuss the specific scaling behavior (dashed curve) in § 3.4.

3.4. Wind Scaling Relations

Equation 35 shows that C_{eff} increases outward provided $v_A/u > 0.64$, which implies that $v_A/u \gtrsim 1$, and in practice $v_A/u \gg 1$ (see Figure 3, Figure 4) for most of the evolution between the footpoint and the critical point.

In the limit of $v_A \gg u$, Equation 23 becomes

$$\frac{\Pi}{\Pi_0} \approx \left(\frac{v_A}{v_{A0}} \frac{A}{A_0} \right)^{-\gamma_{\text{cr}}} = \left(\frac{\rho}{\rho_0} \right)^{\gamma_{\text{cr}}/2} \quad (42)$$

and the effective sound speed (see Equation 28 and Equation 29) becomes

$$C_{\text{eff}}^2 \approx \frac{\gamma_{\text{cr}}}{2} \frac{\Pi_0}{\rho_0} \left(\frac{\rho}{\rho_0} \right)^{\gamma_{\text{cr}}/2-1}. \quad (43)$$

As discussed in § 2.5, this implies that for $\gamma_{\text{cr}} = 4/3$, $C_{\text{eff}}^2 \propto \rho^{-1/3}$, which increases outward as ρ decreases outward.

At the critical point, $C_{\text{eff},c}^2 = V_{g,c}^2 = u_c^2$. Furthermore, since a typical galactic rotation curve is close to flat, $V_{g,c} \sim V_H$ where V_H is a characteristic halo velocity. In particular, Figure 8 shows that the range of ratios $V_{g,c}/V_H = 0.9 - 1.5$ for $V_H = 50 - 300 \text{ km s}^{-1}$. Finally, conservation of mass flux implies $\rho_0 u_0 A_0 = \rho_c u_c A_c$. Combining these relations (and using $\gamma_{\text{cr}} = 4/3$), Equation 43 may be solved for the footpoint mass flux ratio or pressure ratio as

$$\frac{\dot{\Sigma}_c}{\Pi_0} \equiv \frac{u_0 \rho_0 c_s}{\Pi_0} \sim \left(\frac{2}{3} \right)^3 \left(\frac{\rho_0 c_s^2}{\Pi_0} \right)^{-2} \left(\frac{V_H}{c_s} \right)^{-5} \frac{A_c}{A_0} \quad (44)$$

or

$$\frac{\Pi_0}{\rho_0 c_s^2} \sim \frac{3}{2} \left(\frac{V_H}{c_s} \right)^{5/3} \left(\frac{u_0}{c_s} \right)^{1/3} \left(\frac{A_0}{A_c} \right)^{1/3}. \quad (45)$$

Equation 44 shows that for a fixed halo potential (V_H), at large $\rho_0 c_s^2 / \Pi_0$ the normalized mass flux $\dot{\Sigma}_c / \Pi_0$ and footpoint velocity u_0 / c_s must be small. This is consistent with the behavior evident in the numerical wind solution results shown in the top panels of Figure 5 and Figure 6 for $V_H = 50 \text{ km s}^{-1}$ and $V_H = 250 \text{ km s}^{-1}$, respectively. Also, since $u_0 < V_{g,c} \sim V_H$ and $A_0 < A_c$, from Equation 45 a lower limit on the footpoint density is given by $\rho_0 c_s^2 / \Pi_0 \sim (2/3)(V_H/c_s)^{-2}$. This limit is roughly shown with a dashed horizontal line in Figure 5 and Figure 6.

The scaling relation in Equation 45 can be compared to the dependence of the footpoint pressure ratio $\Pi_0 / (\rho_0 c_s^2)$ on V_H and u_0 found in our numerical wind solutions. Figure 9 shows the dependence of $\Pi_0 / (\rho_0 c_s^2)$ on V_H for actual solutions of the wind equation with a series of u_0 values, compared to the analytic estimate Equation 45 taking $A_c/A_0 = 1$. Evidently, the analytic prediction is in quite good agreement with the numerical results. Figure 9 also shows that the solutions are insensitive to the footpoint radius. Dimensional analysis would suggest that if the momentum flux associated with the cosmic ray footpoint pressure, Π_0 , is directly transferred to momentum flux in a wind with characteristic velocity $\sim V_H$ and density $\sim \rho_0$, then one would naively expect $\Pi_0 / \rho_0 \sim V_H^2$. Red lines

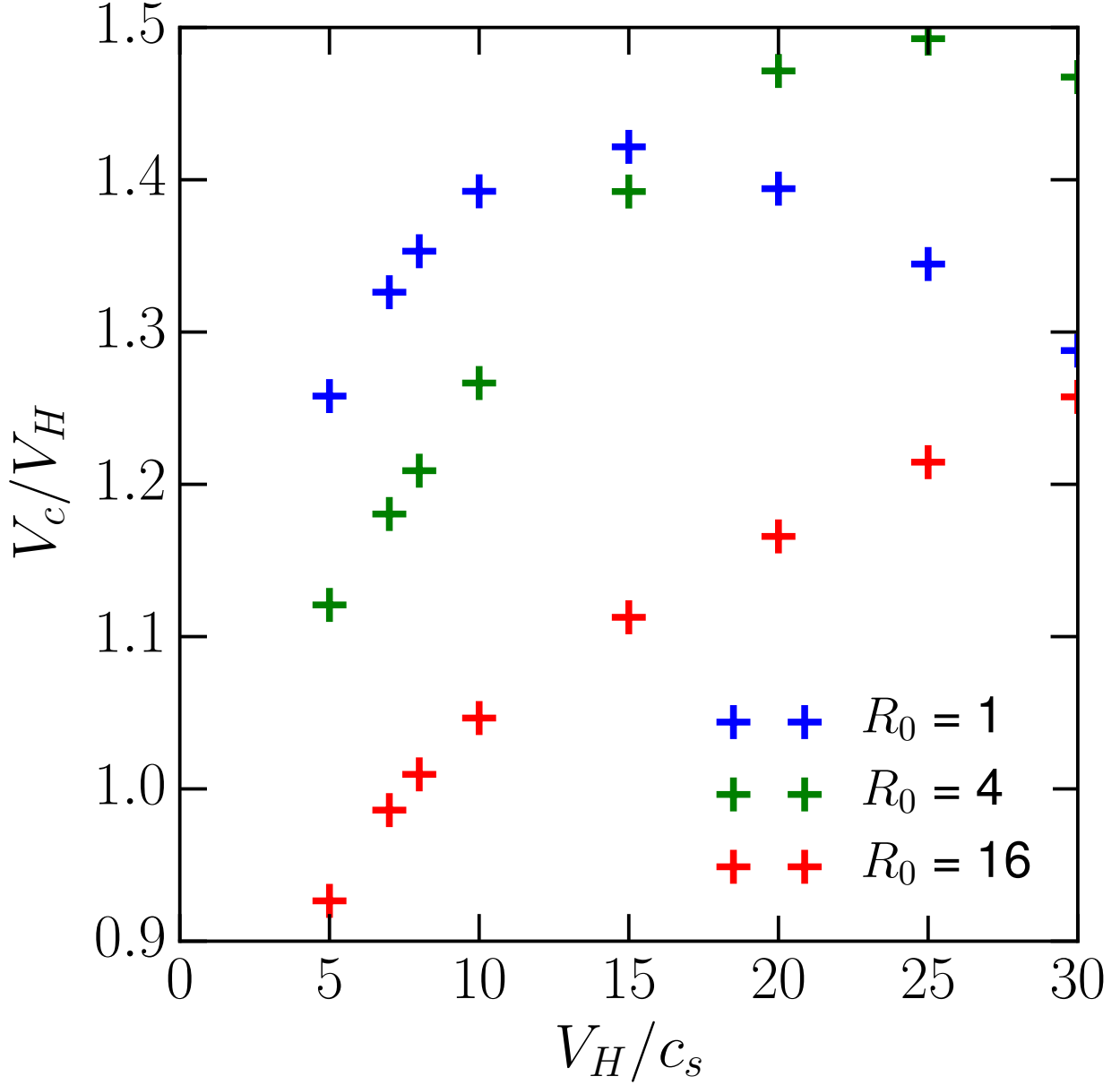


Figure 8. The critical velocity $V_c \equiv u_c = V_{g,c} = C_{\text{eff},c}$ as a function of halo velocity. Parameters are as in Figure 7.

in each panel of Figure 9 shows that this naive expectation is not bad as a zeroth order estimate, but that it increasingly fails to fit the true wind solutions at high V_H and low u_0 . Instead, the prediction $\Pi_0/\rho_0 \sim (3/2)V_H^{5/3}u_0^{1/3}$ of Equation 45 fits the numerical results well over the full parameter space. Similarly, in Figure 10 we compare the results of wind integrations to the predicted dependence of the footpoint pressure ratio on u_0 , again showing good agreement.

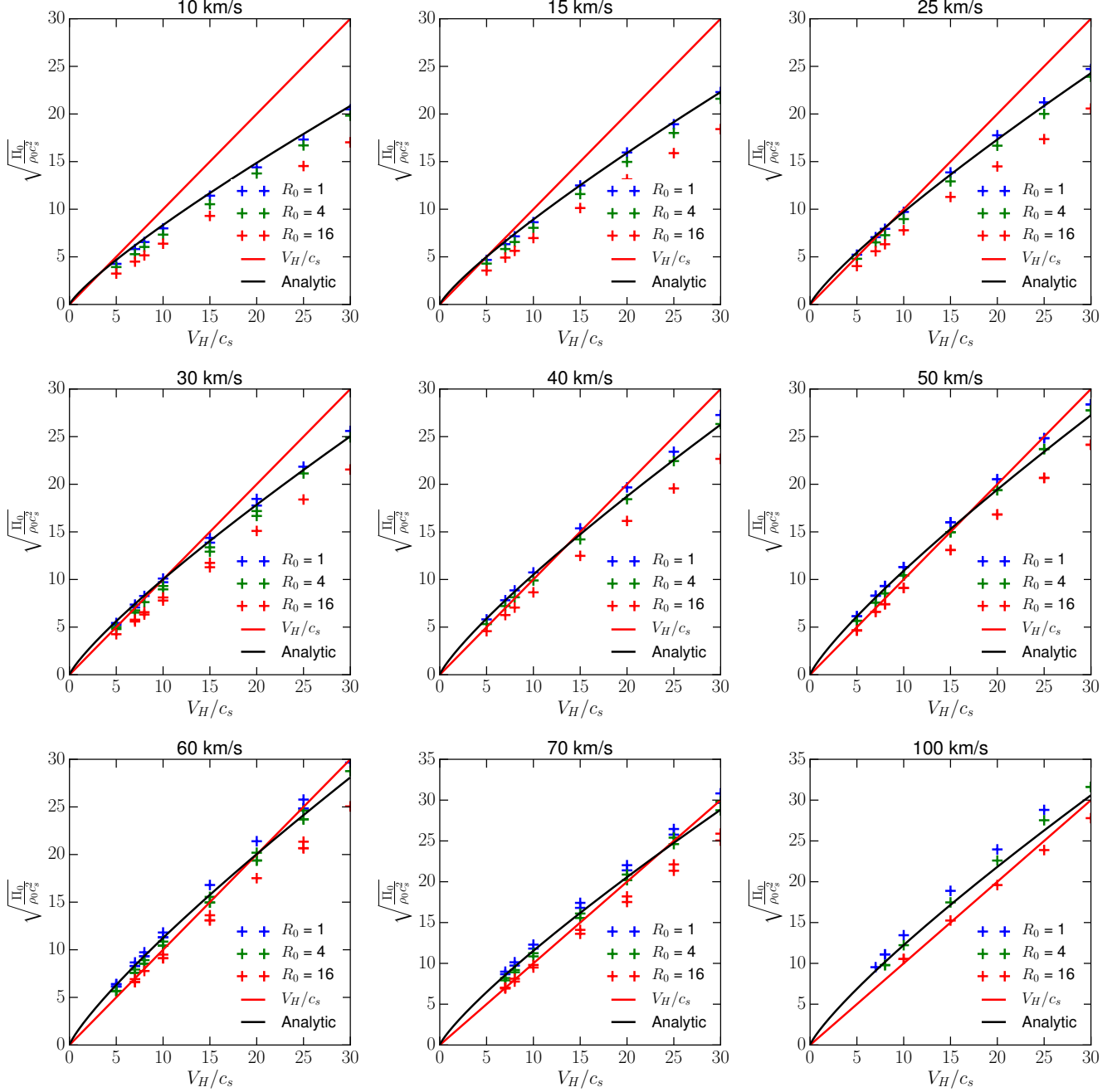


Figure 9. Plots of $\sqrt{\Pi_0/\rho_0 c_s^2}$ from wind solutions with a range of halo potential velocities V_H and footpoint radii R_0 . Other launch conditions are as in Figure 7, except we show results for a range of launch velocities $u_0 = 10 - 100 \text{ km s}^{-1}$ (labeled at top of each panel). In each panel, the red line shows the naive order-of-magnitude estimate ($\Pi_0/\rho_0 \sim V_H^2$), while the black curve labeled “Analytic” shows Equation 45, setting $A_c/A_0 = 1$.

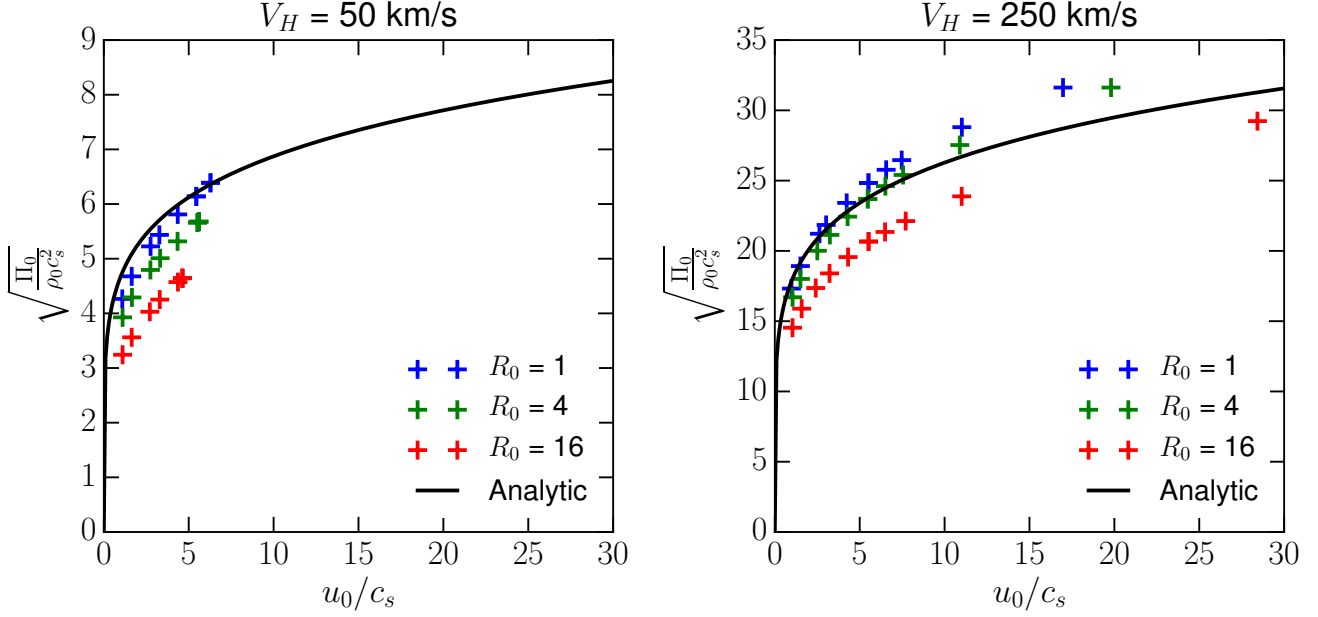


Figure 10. Results for $\sqrt{\Pi_0/\rho_0 c_s^2}$ vs. u_0/c_s , holding V_H fixed. Parameters are otherwise as in Figure 9. The left and right panels show results for a dwarf and massive halo ($V_H = 50 \text{ km s}^{-1}$ and 250 km s^{-1}), respectively. The black curve labeled “Analytic” shows the prediction of Equation 45 with $A_c/A_0 = 1$.

Equation 45 can be rearranged to provide an estimate for the “carrying capacity” mass flux in a galactic disk wind that originates in a coronal region where the cosmic ray pressure is Π_0 and ISM material at $T \sim 10^4 \text{ K}$ is fed from below by a supernova-driven fountain flow with velocity u_0 . This carrying capacity is

$$\dot{\Sigma} = \rho_0 u_0 \sim \frac{2}{3} \Pi_0 V_H^{-5/3} u_0^{2/3} \left(\frac{A_c}{A_0} \right)^{1/3}. \quad (46)$$

Of course, $u_0 < V_{g,c} \sim V_H$, so $\dot{\Sigma} \lesssim \Pi_0/V_H$ for low velocity halos. We compare the carrying capacity to $\dot{\Sigma}_z$ in the top left panel of Figure 7. The difference is at most 10% for $R_0 = 1 \text{ kpc}$, a factor of 2 for $R_0 = 4 \text{ kpc}$, and a factor of 7 for $R_0 = 16 \text{ kpc}$. The variation for different R_0 is primarily due to the geometric factor $\hat{s} \cdot \hat{z}$. For smaller R_0 , the streamline following the gravitational potential starting at $z = 1 \text{ kpc}$ is more vertical, whereas distant R_0 have more radial streamlines.

The relation in Equation 46 shows that winds driven by cosmic ray pressure are not expected to follow either the “momentum” ($\dot{\Sigma}_z \propto V_H^{-1}$) or “energy” ($\dot{\Sigma}_z \propto V_H^{-2}$) scalings that have commonly been adopted in “subgrid” wind models in galaxy formation simulations (Somerville & Davé 2015). Instead, the scaling with V_H is intermediate between these two limits, and an additional dependence on the “feeding” velocity u_0 is also present. We emphasize that the far-field wind velocity *does*, however, scale nearly linearly with V_H , as shown in Figure 7.

Finally, we remark that Equation 46 is the carrying capacity for winds driven by cosmic ray pressure, but more generally for any driving effective pressure P_e , Equation 32 will still hold for $C_{\text{eff}}^2 \rightarrow dP_e/d\rho$ (see Equation 30), and $C_{\text{eff},c}^2 = u_c^2 = V_{g,c}^2$ must still hold at the critical point. If $P_e \propto \rho^{\gamma_e}$, then for a

galactic wind with $V_{g,c} \sim V_H$ the generalization of Equation 46 is

$$\dot{\Sigma} = \rho_0 u_0 \sim \gamma_e P_{e,0} V_H^{-(\gamma_e+1)} u_0^{\gamma_e} \left(\frac{A_c}{A_0} \right)^{1-\gamma_e} \quad (47)$$

where $P_{e,0}$ is the driving pressure at the footpoint. With $C_{\text{eff}}^2 = \gamma_e (P_{e,0}/\rho_0)(\rho/\rho_0)^{\gamma_e-1}$, $0 < \gamma_e < 1$ is required for C_{eff} to increase with distance such that a steady, accelerating wind is able to make a critical transition in a $V_g \sim V_H = \text{const.}$ galactic potential.⁵ Cosmic-ray driven winds have $\gamma_e \approx \gamma_{\text{cr}}/2 = 2/3$ (inside the critical point). Equation 47 shows that any simple pressure-driven galactic disk wind will have dependence on V_H between the “momentum-driven” and “energy-driven” scalings, i.e. $\propto V_H^{-(1+\gamma_e)}$ with $1 < 1 + \gamma_e < 2$. In contrast to case of a galactic disk wind with an extended potential, a wind from a point mass (or any truncated mass distribution) has V_g decreasing outward $\propto r^{-1/2}$, so that a steady wind with a critical transition may have C_{eff} also decrease outward, compatible with $\gamma_e \geq 1$. This is a key distinction between pressure-driven Parker-type winds (which would include quasi-spherical galactic center winds for which the halo potential is unimportant) and galactic disk winds (see Figure 2).

3.5. Angular momentum and magnetic field dependence

Angular momentum of the flow has a small effect on the wind. The centrifugal force produces acceleration in the rotating frame in the \hat{R} direction, and as shown in § 2.1 this effect can be incorporated in an effective potential Ψ . The centrifugal force partly compensates for the inward force of gravity, which near the disk is primarily in the $-\hat{R}$ direction. Since we assume streamlines follow the gradient of the effective potential, and angular momentum reduces the gradient of Ψ in the \hat{R} direction, the resulting streamlines are more vertical at higher J . This effect is shown in Figure 1.

Since angular momentum opposes inward gravitational acceleration, it decreases V_g along the streamline. We do not explore large angular momentum $J > 0.5R_0V_H$ because the effective potential produces a gradient that would be unrealistic for streamlines, turning around towards $R = 0$ at large z .

For a nearly vertical streamline with large J , at $z \gg R$ the gravitational and centrifugal components of the effective potential gradient (which is related to streamline direction $\hat{s} = \nabla\Psi/|\Psi|$ by assumption), respectively drop off as \hat{z}/z and $-\hat{R}R_0^2/R^3$. Since R remains roughly constant and z is increasing, the centrifugal term eventually dominates the streamline. This leads to a streamline which unrealistically turns towards $R = 0$ at large z if $J > J_{\text{max}}$. We numerically determine the maximum value J_{max} for each value of R_0 in Figure 1 and note that typically $J_{\text{max}} > 0.5R_0V_H$. Hence, we avoid those values. This consideration determines the range of streamlines depicted in Figure 1.

For given mass flux $\dot{\Sigma} = \rho_0 u_0$ along streamlines, the mass-loss rate per unit area in the disk $\dot{\Sigma}_z$ is lower by a factor $\hat{s} \cdot \hat{z} = [(dR/dz)^2 + 1]^{-1/2}$. More vertical streamlines, with smaller dR/dz , therefore have a larger $\dot{\Sigma}_z$, other things being equal. By examining Figure 1, this effect is small for small footpoint radii R_0 , since the fractional change in $\hat{s} \cdot \hat{z}$ is small for varying J .

Figure 11 shows results for mass-loss rates in two different halo potentials, at a range of footpoint locations, for varying angular momentum parameter J . The top panels show that the mass-loss rate

⁵ Note that we find $V_g \sim V_H$ for disk winds with footpoints and critical points at scales $\sim 1 - 10$ kpc. For galactic center quasi-spherical winds with critical points at smaller scales (~ 200 pc), Bustard et al. (2016, 2017) find that the halo component can be neglected. In this case $V_g \sim V_H$ does not hold so Equation 47 does not apply and $\gamma < 1$ is not required for a wind.

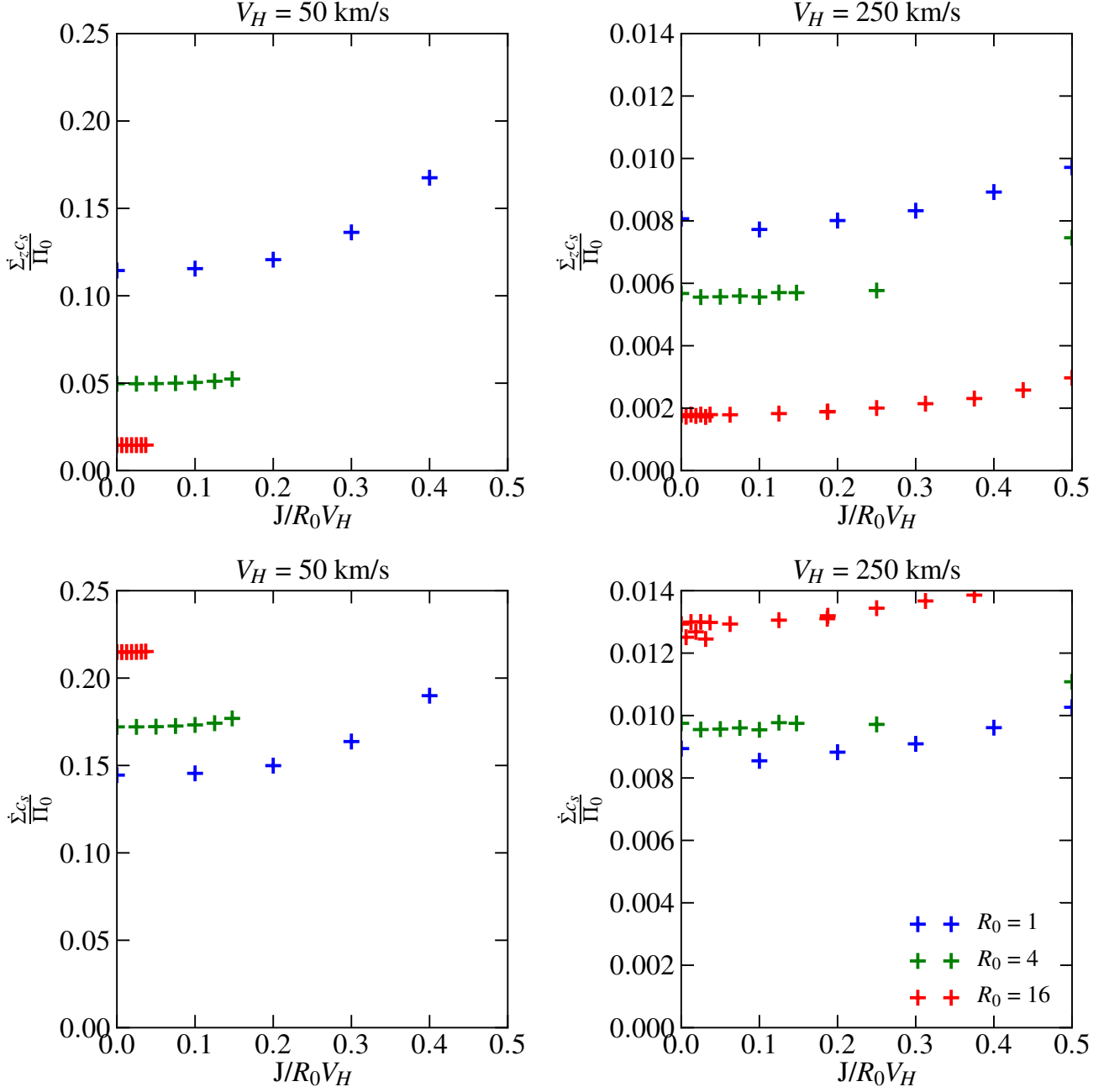


Figure 11. Dependence of streamline flux $\dot{\Sigma} = \rho_0 u_0$ and disk mass-loss rate per unit area $\dot{\Sigma}_z = \hat{s} \cdot \hat{z} \dot{\Sigma}$ on the angular momentum parameter J . Top: $\dot{\Sigma}_z c_s / \Pi_0$ vs. $J/(R_0 V_H)$. Bottom: $\dot{\Sigma}_{c_s} / \Pi_0$ vs. $J/(R_0 V_H)$. Left panels show results from a dwarf galaxy potential ($V_H = 50$ km s $^{-1}$) and right panels show results from a Milky Way-like potential ($V_H = 250$ km s $^{-1}$). For all cases, $\Pi_0 = B_0^2 / 8\pi$ and $u_0 = 50$ km s $^{-1}$ at the footpoint at height $z_0 = 1$ kpc. Points with different colors correspond to streamlines with footpoint radii $R_0 = 1, 4, 16$ kpc. The mass-loss rate increases slightly with J , but overall the effect of rotation is modest.

per unit area in the disk depends more strongly on R_0 (and corresponding streamline geometry) than on the angular momentum J . The bottom panels show that larger R_0 cases correspond to larger $\dot{\Sigma}$ (because V_g is slightly smaller at the critical point; see § 3.4). In comparison, the top panels show that the geometric effect is strong enough to reverse this trend for $\dot{\Sigma}_z = \hat{s} \cdot \hat{z} \dot{\Sigma}$, with larger R_0 yielding smaller $\dot{\Sigma}_z$. Note that increasing J decreases the upper limit on u_0 for which there is an accelerating solution. For example, at large values of $J/R_0 V_H$ and fixed $u_0 = 50 \text{ km s}^{-1}$, accelerating solutions exist for high V_H halos but not low V_H halos, as evident in Figure 11.

In this work, we have ignored the toroidal component of the magnetic field and any associated magnetic stresses. Work by Zirakashvili et al. (1996) includes these magnetic forces in a rotating galaxy, finding that increasing the magnetic field strength by a factor of 3 leads to roughly 1.4 - 2 times more mass loss. If we included magnetic forces, they would provide an additional acceleration that could increase u^2 up to $u_\phi^2/(1 - M_A^2)$, where $M_A = u/v_A$. Both M_A and u_ϕ are small inside the critical point for the winds we study so the acceleration from magnetic pressure forces would be small.

Since we do not include magnetic forces, the magnetic field only affects winds through the value of the Alfvén speed v_A (associated with the poloidal field component), which controls the streaming rate of cosmic rays. This in turn affects the evolution of C_{eff} , which must increase relative to V_g to produce a critical point where $C_{\text{eff}} = V_g$. To have C_{eff} increase outward, $v_A/u > 0.64$ is required (see Equation 35). Since v_A relative to u only determines the effective adiabatic index of the cosmic ray fluid, v_A does not directly appear in the scaling relation Equation 45 (for sufficiently large v_A), and therefore the wind is expected to depend only weakly on the strength of the magnetic field B . We find that in wind solutions the magnetic field strength at the base of the flow (B_0) indeed has a relatively small effect on the wind properties. This is evident in Figure 12, in which changing the magnetic pressure by three orders of magnitude leads to less than order unity change in the mass loss rate. This is also evident in the top left panel of Figure 5 and Figure 6. At smaller magnetic field strengths, increasing B_0 leads to increased mass loss since a larger v_A allows a larger u_0 under the constraint that v_A/u must be large enough to produce an accelerating wind with a sonic transition.

3.6. Implications for Mass Loading of Galactic Winds

Mass fluxes for our wind solutions are all given in units of Π_0/c_s , with values in the range $\sim 0.001 - 0.1$ in these units (see Figure 5, Figure 6, Figure 7, Figure 11, Figure 12). The physical value of the mass flux therefore depends on the cosmic ray pressure (or energy density) in the region where the wind originates. Consider as an example the Solar neighborhood, where the local cosmic ray pressure is $P_{\text{cr}} \sim 0.6 \text{ eV cm}^{-3}$ (Grenier et al. 2015). Using $c_s = 10 \text{ km s}^{-1}$, the dimensional factor for the mass-loss rate would be $\Pi_0/c_s \rightarrow P_{\text{cr}}/10 \text{ km s}^{-1} \sim 0.15 M_\odot \text{ kpc}^{-2} \text{ yr}^{-1}$. For $\dot{\Sigma}_z c_s/\Pi_0 \sim 0.004$, as might be appropriate for the Solar neighborhood with $u_0 = 50 \text{ km s}^{-1}$ (see Figure 7), the result is $\dot{\Sigma}_z \sim 5 \times 10^{-4} M_\odot \text{ kpc}^{-2} \text{ yr}^{-1}$. The corresponding footpoint number density of the wind at $z = 1 \text{ kpc}$ would be $n_0 = 8 \times 10^{-4} \text{ cm}^{-3}$ (assuming mean molecular weight of $1.4 m_H$). This mass-loss rate is $\sim 20\%$ of the observed star formation rate estimated in the Solar neighborhood, $2.5 \times 10^{-3} M_\odot \text{ kpc}^{-2} \text{ yr}^{-1}$ (Fuchs et al. 2009).

More generally, we showed that the “carrying capacity” estimate in Equation 46 follows the numerical results quite well, especially for small R_0 (see Figure 7), so it is useful to rewrite it in dimensional

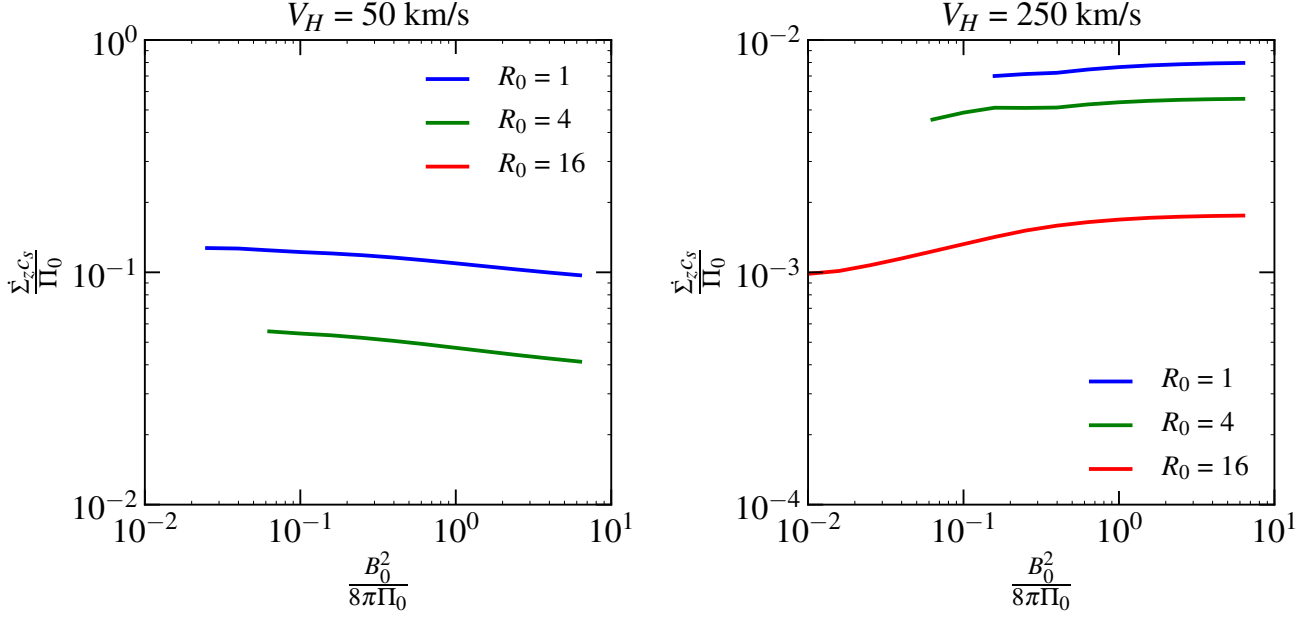


Figure 12. Mass-loss rate per unit area $\dot{\Sigma}_z c_s / \Pi_0$ vs. magnetic pressure $B_0^2 / 8\pi \Pi_0$ for $u_0 = 50$ km/s in a dwarf galaxy potential with $V_H = 50$ km s $^{-1}$ and a Milky-Way like potential with $V_H = 250$ km s $^{-1}$. Winds originate from $z_0 = 1$ kpc and $R_0 = 1, 4, 16$ kpc with no angular momentum ($J = 0$). The mass loss rate varies only very weakly with magnetic field strength.

form (with $A_c/A_0 = 1$) as

$$\dot{\Sigma} \sim 3 \times 10^{-3} M_\odot \text{ kpc}^{-2} \text{ yr}^{-1} \left(\frac{\Pi_0}{1 \text{ eV cm}^{-3}} \right) \left(\frac{V_H}{200 \text{ km s}^{-1}} \right)^{-5/3} \left(\frac{u_0}{50 \text{ km s}^{-1}} \right)^{2/3}. \quad (48)$$

Lower halo velocity V_H or higher feeding velocity u_0 increases the mass-loss rate. The corresponding density of hydrogen nuclei in the wind at the footpoint in the launching region (above the main ISM disk) is

$$n_0 \sim 1.8 \times 10^{-3} \text{ cm}^{-3} \left(\frac{\Pi_0}{1 \text{ eV cm}^{-3}} \right) \left(\frac{V_H}{200 \text{ km s}^{-1}} \right)^{-5/3} \left(\frac{u_0}{50 \text{ km s}^{-1}} \right)^{-1/3}. \quad (49)$$

Note that this density is much lower than the typical midplane density of both the cold and warm ISM, but based on numerical simulations (e.g. Kim & Ostriker 2017, submitted) is similar to mean densities of warm “fountain” gas in galactic disk corona regions.

Mass-loss in galactic winds is often characterized in terms of the “mass loading,” defined as the ratio of the local wind mass-loss rate to the local star formation rate, $\beta \equiv \dot{\Sigma}_{\text{wind}} / \Sigma_{\text{SFR}}$, where $\dot{\Sigma}_{\text{wind}} = \dot{\Sigma}_z$ in the present notation. Because cosmic rays are produced in the supernova remnants associated with explosions from young, massive stars, the cosmic ray pressure at the disk midplane likely scales with the star formation rate, $P_{\text{cr}} = \eta_{\text{cr}} \Sigma_{\text{SFR}}$. For the Solar neighborhood, $\eta_{\text{cr}} \sim 600$ km s $^{-1}$. Other components of the midplane pressure, including the thermal pressure and turbulent kinetic and magnetic pressures, are expected to be proportional to Σ_{SFR} (Ostriker et al. 2010; Ostriker & Shetty 2011) with respective “feedback yield” coefficients η_{th} , η_{turb} , $\eta_{\delta B}$, etc., that can be computed with

detailed numerical simulations of the ISM including star formation and feedback (Kim et al. 2011, 2013; Kim & Ostriker 2015, 2016), such that the total pressure is $P_{\text{tot}} = \eta_{\text{tot}} \Sigma_{\text{SFR}}$.

Assuming Π_0 is comparable to the midplane cosmic ray pressure, we then have for the predicted mass-loading factor for cosmic-ray driven winds,

$$\frac{\dot{\Sigma}_{\text{wind,cr}}}{\Sigma_{\text{SFR}}} = \frac{\eta_{\text{cr}}}{c_s} \frac{\dot{\Sigma}_z c_s}{\Pi_0} \quad (50)$$

$$\sim 0.8 \left(\frac{\eta_{\text{cr}}}{600 \text{ km s}^{-1}} \right) \left(\frac{V_H}{200 \text{ km s}^{-1}} \right)^{-5/3} \left(\frac{u_0}{50 \text{ km s}^{-1}} \right)^{2/3} \left(\frac{A_c}{A_0} \right)^{1/3} \hat{z} \cdot \hat{s}. \quad (51)$$

In applying Equation 50, numerical results for $\dot{\Sigma}_z c_s / \Pi_0$ can be drawn from the figures, while Equation 51 comes from Equation 46. Assuming $\eta_{\text{cr}} / c_s \sim 100$, the mass-loading factor for cosmic-ray driven winds will exceed unity when $\dot{\Sigma}_z c_s / \Pi_0 \gtrsim 0.01$. From the top-left panels of Figure 5 and Figure 6, the mass loading is order unity or higher near equipartition ($B_0^2 / 8\pi \Pi_0 \sim 1$) for sufficiently low ρ_0 , which corresponds to high u_0 (top-right panels of Figure 5 and Figure 6). From Equation 51, mass-loading for cosmic-ray driven winds is expected to exceed unity in dwarf galaxies where $V_H \lesssim 200 \text{ km s}^{-1}$, provided $u_0 \sim 50 \text{ km s}^{-1}$ is consistent with galactic fountain flows that carry gas into the corona (see e.g. Kim & Ostriker 2017, submitted).

Finally, we emphasize that Equations 46, 48, and 50 represent carrying capacities, and hence are upper limits for the mass flux or mass-loading of a cosmic-ray driven warm-gas wind that originates in disk corona regions and is fed by a galactic fountain from below. Of course, the wind mass-loss rate cannot exceed the mass feeding rate from below. While the general dependence of the fountain mass flux on local disk parameters is not presently known, current numerical MHD simulations of supernova-driven outflows do show a mass-loading factor of the warm fountain near unity at height of a few times the warm-ISM scale height (Kim & Ostriker 2017, submitted; see also Martizzi et al. (2016) and Li et al. (2017)).

The asymptotic specific energy of the gaseous wind is $(1/2)V_\infty^2$, where $V_\infty / V_H \sim 2$ from Figure 7. This implies that the asymptotic energy loading of the wind (defined as ratio of wind energy to energy injected by supernovae) is then $\sim (V_H / 500 \text{ km s}^{-1})^2$ times the mass-loading factor, where we have assumed $100 M_\odot$ in stars are formed for every 10^{51} erg of energy injected by supernovae. Using the fiducial η_{cr} and u_0 in Equation 51, this yields an energy loading less than $\sim 10\%$ for $V_H < 300 \text{ km s}^{-1}$, as must be the case if the wind ultimately derives its power from cosmic rays that are accelerated in supernova remnants. However, we caution that η_{cr} in Equation 51 need not be a constant, and it is not known how it may depend on local ISM properties. The energy flux in cosmic rays at the base of the wind is $(u_0 + v_{A,0}) 3 \Pi_0 \hat{z} \cdot \hat{s}$. If we assume that this is of order 10% of the energy input rate from supernovae, $(700 \text{ km s}^{-1})^2 \Sigma_{\text{SFR}}$, this places a practical upper limit on the product $(u_0 + v_{A,0}) \eta_{\text{cr}} \hat{z} \cdot \hat{s}$.

4. SUMMARY AND DISCUSSION

In this paper, we have used one-dimensional (1D) steady-state models to explore the properties of galactic disk winds driven by cosmic ray pressure. In contrast to previous studies of cosmic-ray driven disk winds using steady-state 1D idealizations (Ipavich 1975; Breitschwerdt et al. 1991), we adopt a streamline shape that is specifically motivated by “downhill” flow in a realistic galactic effective potential (including bulge, disk, halo, and a centrifugal term). Also, as our main interest is in understanding how large quantities of relatively cold gas may be accelerated to escape from a deep

potential well, we adopt an isothermal equation of state with $c_s = 10 \text{ km s}^{-1}$ ($T \sim 10^4 \text{ K}$) for which thermal pressure forces are negligible and cosmic ray pressure forces provide the needed acceleration, rather than considering hot outflows (as from galactic center starburst regions) that are driven by both thermal and cosmic ray pressure (e.g. [Everett et al. 2008](#)).

A key feature of winds driven by cosmic ray pressure is that the square of the effective sound speed $C_{\text{eff}}^2 = d\Pi/d\rho$ increases $\propto \rho^{-1/3}$ with decreasing ρ when v_A/u is sufficiently large (see [Equation 35](#) and [§ 3.4](#)), and generally increases relative to the squared gravitational velocity $V_g^2 = d_s\Psi/d_s \ln A$ inside the critical point (see [Appendix B](#)). In contrast, an adiabatic thermal wind cools as it expands and ρ drops, so that the sound speed strictly decreases outward as $C_{\text{eff}}^2 \propto \rho^{\gamma_e-1}$ for $\gamma_e > 1$. Thermal-pressure driven galactic disk winds face an inherent challenge, as V_g must decrease faster than C_{eff} in order to make a steady sonic transition, but a galactic potential including an extended dark matter halo has a nearly flat rotation curve with $V_g^2 \sim V_H^2$ out to large radii. For cosmic rays, C_{eff}^2 increases outward because streaming at the Alfvén speed implies $\Pi \propto n_{\text{cr}}^{\gamma_{\text{cr}}} \propto (v_A A)^{-\gamma_{\text{cr}}} \propto \rho^{\gamma_{\text{cr}}/2} \propto \rho^{2/3}$. [Figure 2](#) shows the characteristic differences between galactic winds driven by cosmic ray pressure and classical Parker stellar winds, while [Figure 3](#) and [Figure 4](#) show examples of our full numerical solutions.

We performed a wide parameter exploration over halo virial velocities $V_H = 50 - 300 \text{ km s}^{-1}$ (masses $M_H \sim 10^{10} - 10^{12} M_\odot$), streamline footpoint radii $R_0 = 1 - 16 \text{ kpc}$, angular momentum $J = 0 - 0.5 R_0 V_H$, ratios of footpoint magnetic pressure to cosmic ray pressure $B_0^2/(8\pi\Pi_0) = 10^{-3} - 10$, and ratios of footpoint gas pressure to cosmic ray pressure $\rho_0 c_s^2/\Pi_0 = 10^{-3} - 10$.

Our steady wind solutions have the following properties:

1. Winds are sub-Alfvénic ($u < v_A$) at least until reaching the critical point (see [Appendix B](#)). After making a sonic transition, where $C_{\text{eff},c} = u_c = V_{g,c} \sim V_H$, acceleration slows and u flattens out, while v_A declines rapidly and C_{eff} declines slowly at large distance.
2. For fixed u_0 , the dimensionless mass-loss rate $\rho_0 u_{0,z}/\Pi_0$ is insensitive to the footpoint magnetic-to-cosmic-ray pressure ratio $B_0^2/(8\pi\Pi_0)$ and angular momentum ([Figure 11](#), [Figure 12](#)). The value of $\rho_0 u_{0,z}/\Pi_0$ increases at low gas-to-cosmic-ray pressure ratio $\rho_0 c_s^2/\Pi_0$ ([Figure 5](#), [Figure 6](#)). However, the solution space for steady, accelerating winds to exist at all has a minimum footpoint gas density, corresponding to $\Pi_0/V_H^2 \lesssim \rho_0$.
3. For $B_0^2/(8\pi\Pi_0) = 1$ and footpoint velocity $u_0 = 50 \text{ km s}^{-1}$, over the full range of V_H we find that the mass-loss rate $\dot{\Sigma}_z = \rho_0 u_{0,z} \sim 0.01 - 0.1 \Pi_0$ (decreasing at larger V_H and increasing slightly with R_0), the critical point is close to the disk $z_c \sim 1 - 5 \text{ kpc}$ (increasing linearly with V_H) with $v_{A,c} \sim V_H$, and at the virial radius u is 2 - 3 times V_H ([Figure 7](#)).

We show that our numerical integration results are in good agreement with a simple analytic prediction relating footpoint properties of “successful” steady wind solutions with the halo velocity as $\Pi_0/(\rho_0 u_0^{1/3}) \sim (3/2)V_H^{5/3}$, as given in [Equation 45](#). This can be recast as the carrying capacity of a wind driven by cosmic ray pressure, with streamline mass flux $\dot{\Sigma} \sim (2/3)\Pi_0 V_H^{-5/3} u_0^{2/3}$ ([Equation 46](#) or [Equation 48](#)). The footpoint velocity u_0 that enters the mass-loss estimate is presumably limited by the supernova-driven fountain flow that carries gas from the midplane to the “coronal” region above the disk. For galaxies with potentials similar to the Milky Way, [Equation 51](#) suggests that the mass-loss rates for winds driven by cosmic ray pressure will be only slightly lower than the star formation rates. Mass loss could significantly exceed star formation for dwarf galaxies.

An interesting feature of cosmic ray driven winds is their dependence on the halo velocity. Whereas nominally the wind mass loading $\beta = \dot{\Sigma}_{\text{wind}}/\dot{\Sigma}_{\text{SFR}} \propto V_H^{-1}$ for “momentum driven” winds and $\beta \propto V_H^{-2}$ for “energy driven” winds (Murray et al. 2005; Somerville & Davé 2015), Equation 51 argues that $\beta \propto V_H^{-5/3}$ for galactic disk winds driven by cosmic ray pressure. This power law is in between the “momentum” and “energy” scalings, is intriguingly similar to that in observations by Chisholm et al. (2017), and is also consistent with other observations (see § 1). We remark that more generally, steady galactic disk winds driven by any gamma-law pressure force would have $\beta \propto V_H^{-(\gamma_e+1)}$ for $0 < \gamma_e < 1$.

Our work has several limitations. For example, we do not include cosmic ray diffusion, and we do not include effects of magnetic pressure or tension forces on the flow. We also do not model the winds from a full disk but rather individual non-interacting streamlines. A full disk would have non-uniform structure and a distribution of cosmic ray pressures, gas densities, and launching velocities from gas motions. Our model is unable to incorporate possible effects of interaction between streamlines. Furthermore, we treat the gas as a single-phase medium, but in reality the warm medium in galactic disk coronal regions at $z \gtrsim \text{kpc}$ would have a volume filling factor below unity, with “warm fountain” gas intermixed with hot gas (e.g. Kim & Ostriker 2017, submitted). The effects of volume filling factor on mass loss are uncertain, especially as cosmic ray pressure forces on the gas are mediated by the interaction of both the cosmic rays and gas with magnetic fields. To move beyond these limitations will require full numerical MHD simulations of a multiphase ISM, including self-consistent star formation and feedback, with a cosmic ray treatment that includes streaming at the Alfvén speed along magnetic field lines.

While our models are idealized in many respects, our results provide evidence that cosmic-ray driven winds may be quite important to the evolution of galaxies, especially at $V_H \lesssim 200 \text{ km s}^{-1}$. Our analysis makes clear the distinctive physics behind cosmic-ray driven winds, also providing scaling relations that may prove useful for tests of and comparisons to fully three-dimensional numerical implementations. With the possibility that cosmic ray pressure may drive more mass out of dwarf galaxies than is locked up in stars, there is strong motivation to include a realistic treatment of cosmic rays in future galaxy formation simulations.

ACKNOWLEDGMENTS

We are grateful to the referee, Ellen Zweibel, for an insightful report, and Eliot Quataert for helpful suggestions. This work was supported by the National Science Foundation under grant AST-1312006 and NASA under grant NNX17AG26G to ECO, and grant DGE-1148900 providing a Graduate Research Fellowship to SAM.

APPENDIX

A. ION NEUTRAL DAMPING

To estimate the effect of ion-neutral damping we compare the streaming instability growth rate with the ion neutral damping rate. The growth rate is (Kulsrud & Pearce 1969):

$$\Gamma_{\text{CR}} \sim \Omega_0 \frac{n_{\text{CR}}}{n_{\text{i}}} \left(\frac{v_{\text{D}}}{v_{\text{A}}} - 1 \right) \quad (\text{A1})$$

for ion cyclotron frequency Ω_0 , cosmic ray number density n_{CR} , ion number density n_i (corresponding to mass density $\rho = \mu n_i$), and mean drift velocity of the cosmic ray distribution v_D . We write $f_D = ((v_D/v_A) - 1)$.

We note that

$$\frac{n_{\text{CR}}}{n_i} \sim \frac{\Pi}{\rho c^2} \quad (\text{A2})$$

and use Equation 45 so that at the base of the wind

$$\Gamma_{\text{CR}} \sim \Omega_0 \left(\frac{V_H}{c} \right)^{5/3} \left(\frac{u_0}{c} \right)^{1/3} f_D. \quad (\text{A3})$$

The damping rate is (Kulsrud & Pearce 1969):

$$\Gamma_{\text{in}} = \frac{1}{2} n_n \langle \sigma v \rangle \quad (\text{A4})$$

for neutral number density n_n and rate coefficient $\langle \sigma v \rangle$, where we assume a mostly-ionized medium. From Kulsrud & Cesarsky (1971), $\langle \sigma v \rangle = 1.53$ to $8.40 \times 10^{-9} \text{ cm}^3 \text{ s}^{-1}$ for $T = 100$ to 10^4 K .

Setting $\Gamma_{\text{CR}} > \Gamma_{\text{in}}$ as the condition for ion neutral damping to be ignored, this requires

$$n_n f_D^{-1} \lesssim 3 \text{ cm}^{-3} \left(\frac{B}{\mu\text{G}} \right) \left(\frac{V_H}{200 \text{ km s}^{-1}} \right)^{5/3} \left(\frac{u_0}{50 \text{ km s}^{-1}} \right)^{1/3} \left(\frac{\langle \sigma v \rangle}{10^{-9} \text{ cm}^3 \text{ s}^{-1}} \right)^{-1} \quad (\text{A5})$$

This says that ion-neutral damping may be neglected provided that n_n/f_D is not too large. If n_n is small, that means that f_D can also be very small (i.e. $v_D \rightarrow v_A$); larger n_n would require larger drift. A lower estimate, taking $f_D \sim 1$, $V_H = 50 \text{ km s}^{-1}$, and a rate coefficient of $10^{-8} \text{ cm}^3 \text{ s}^{-1}$, gives $n_n \lesssim 0.03 \text{ cm}^{-3}$. This is easily satisfied for the parameter regime we consider, since even the ion density is only $\sim 10^{-3} \text{ cm}^{-3}$ for $\dot{\Sigma}_z \sim 10^{-3} M_\odot \text{ kpc}^{-2} \text{ yr}^{-1}$ (see also Equation 49 more generally). The mass-loss rate would have to be very high, and the neutral fraction very large, for ion-neutral damping to be significant.

Finally, we note that for primarily-neutral gas in higher density clouds, ion-neutral collisional damping is much stronger and cosmic rays are therefore expected to stream rapidly through such clouds, whether within the ISM or in galactic winds (Everett & Zweibel 2011).

B. EFFECTIVE SOUND SPEED

By combining Equation 22, Equation 23, Equation 24, Equation 25, and Equation 28, the effective sound speed can be written purely as a function of ρ and the ratio v_A/u . Then, using $d(u/v_A)/d \ln \rho = -(1/2)u/v_A$, we have

$$\frac{1}{(C_{\text{eff}}^2 - c_s^2)} \frac{dC_{\text{eff}}^2}{d \ln \rho} = \frac{\gamma_{\text{cr}} \left(1 + \frac{1}{2} \frac{v_A}{u} \right)^2 - 1 - \frac{7}{4} \frac{v_A}{u} - \frac{1}{2} \frac{v_A^2}{u^2}}{\left(1 + \frac{v_A}{u} \right) \left(1 + \frac{v_A}{2u} \right)}. \quad (\text{B6})$$

Since $C_{\text{eff}}^2 - c_s^2$ is positive and $d_s \ln \rho < 0$ (ρ decreases outward), C_{eff} will increase outward ($d_s C_{\text{eff}}^2 > 0$) provided that the sign of the right-hand side is negative. For $\gamma_{\text{cr}} = 4/3$, this is true for $v_A/u > 0.64$.

The linear dependence of ρ^{-1} on u and A also allows us to simplify our treatment of the sonic transition (§ 2.4) from Equation 36. That is, $(d_s A) \partial_A = (A d_s \ln A) \partial_A = (A d_s \ln A) (\partial_A \rho^{-1}) \partial_{\rho^{-1}} =$

$-(d_s \ln A) \partial_{\ln \rho}$. Similarly, $\partial_u = (\rho^{-1}/u) \partial_{\rho^{-1}} = -(1/u) \partial_{\ln \rho}$. The partial derivatives with respect to u assume holding A constant and vice versa. Solving Equation 36 for $d_s u$, the behavior of the wind at the critical transition is then given by a quadratic

$$0 = ((-1/u) \partial_{\ln \rho} C_{\text{eff}} - 1)(d_s u)^2 - 2 \partial_{\ln \rho} C_{\text{eff}} d_s \ln A (d_s u) - u d_s \ln A (\partial_{\ln \rho} C_{\text{eff}} d_s \ln A - d_s V_g) \quad (\text{B7})$$

$$\equiv a(d_s u)^2 + b(d_s u) + c$$

with a solution

$$d_s u = \frac{b}{-2a} + \frac{\sqrt{b^2 - 4ac}}{-2a}. \quad (\text{B8})$$

Since C_{eff} changes slowly, $a < 0$. Hence, there is an accelerating wind passing through the sonic point whenever $b > 0$ so that $d_s u > 0$. This corresponds to when $\partial_{\rho^{-1}} C_{\text{eff}} > 0$. However, it is also possible to attain $d_s u > 0$ when $b < 0$, as long as $-4ac > 0$, so that the determinant is larger than b . This corresponds to $-\partial_{\ln \rho} C_{\text{eff}} d_s \ln A > d_s V_g$. This is simply a mathematical demonstration of the qualitative property that the wind begins with $u_0 < C_{\text{eff},0} < V_{g,0}$ and evolves so that eventually $V_g < C_{\text{eff}} < u$. In order for C_{eff} and V_g to change order, C_{eff} must increase relative to V_g . This concept is roughly illustrated in Figure 2. For a typical galactic potential with a nearly flat rotation curve, V_g slightly decreases and is nearly constant. Thus, it is sufficient for $-\partial_{\ln \rho} C_{\text{eff}} > 0$, so at the critical transition point, it is necessary for $v_A \gtrsim 0.64u$. Before this point, since v_A/u is strictly decreasing, $v_A \gtrsim u$ throughout the evolution of an accelerating wind with a smooth sonic transition.

Another possible family of accelerating solutions to Equation B7 under the assumption $a < 0$ is

$$d_s u = \frac{b}{-2a} - \frac{\sqrt{b^2 - 4ac}}{-2a}. \quad (\text{B9})$$

This requires $b > 0$ so that $-\partial_{\ln \rho} C_{\text{eff}} > 0$ and hence $d_s C_{\text{eff}} > 0$, and simultaneously $-4ac < 0$, so that $d_s V_g > -\partial_{\ln \rho} C_{\text{eff}} (d_s \ln A) > 0$. Again, since $b > 0$, this leads to $v_A \gtrsim u$. For such sonic point conditions, two branches of solutions are possible, but this second branch of solutions only occurs for gravitational potentials where V_g is increasing.

REFERENCES

- Anderson, M. E., & Bregman, J. N. 2010, *ApJ*, 714, 320
- Behroozi, P. S., Wechsler, R. H., & Conroy, C. 2013, *ApJ*, 770, 57
- Bell, A. R. 2004, *MNRAS*, 353, 550
- Bell, E. F., McIntosh, D. H., Katz, N., & Weinberg, M. D. 2003, *ApJL*, 585, L117
- Booth, C. M., Agertz, O., Kravtsov, A. V., & Gnedin, N. Y. 2013, *ApJL*, 777, L16
- Bovy, J. 2015, *ApJS*, 216, 29
- Breitschwerdt, D., McKenzie, J. F., & Voelk, H. J. 1991, *A&A*, 245, 79
- Bustard, C., Zweibel, E. G., & Cotter, C. 2017, *ApJ*, 835, 72
- Bustard, C., Zweibel, E. G., & D’Onghia, E. 2016, *ApJ*, 819, 29
- Cen, R., & Ostriker, J. P. 1999, *ApJ*, 514, 1
- Chen, H.-W. 2012, *MNRAS*, 427, 1238
- Chevalier, R. A., & Clegg, A. W. 1985, *Nature*, 317, 44
- Chisholm, J., Tremonti, C. A., Leitherer, C., & Chen, Y. 2017, *MNRAS*, 469, 4831
- Chisholm, J., Tremonti, C. A., Leitherer, C., et al. 2015, *ApJ*, 811, 149
- Everett, J. E., & Zweibel, E. G. 2011, *ApJ*, 739, 60
- Everett, J. E., Zweibel, E. G., Benjamin, R. A., et al. 2008, *ApJ*, 674, 258

- Ferrière, K. M. 2001, *Reviews of Modern Physics*, 73, 1031
- Fuchs, B., Jahreiß, H., & Flynn, C. 2009, *AJ*, 137, 266
- Grenier, I. A., Black, J. H., & Strong, A. W. 2015, *ARA&A*, 53, 199
- Haffner, L. M., Dettmar, R.-J., Beckman, J. E., et al. 2009, *Reviews of Modern Physics*, 81, 969
- Hanasz, M., Lesch, H., Naab, T., et al. 2013, *ApJL*, 777, L38
- Heckman, T. M., Alexandroff, R. M., Borthakur, S., Overzier, R., & Leitherer, C. 2015, *ApJ*, 809, 147
- Heckman, T. M., & Borthakur, S. 2016, *ApJ*, 822, 9
- Heckman, T. M., & Thompson, T. A. 2017, *ArXiv e-prints*, arXiv:1701.09062
- Ipavich, F. M. 1975, *ApJ*, 196, 107
- Kim, C.-G., Kim, W.-T., & Ostriker, E. C. 2011, *ApJ*, 743, 25
- Kim, C.-G., & Ostriker, E. C. 2015, *ApJ*, 815, 67
- . 2016, *ArXiv e-prints*, arXiv:1612.03918
- Kim, C.-G., Ostriker, E. C., & Kim, W.-T. 2013, *ApJ*, 776, 1
- Kim, C.-G., Ostriker, E. C., & Raileanu, R. 2017, *ApJ*, 834, 25
- Kulsrud, R., & Pearce, W. P. 1969, *ApJ*, 156, 445
- Kulsrud, R. M. 2005, *Plasma physics for astrophysics*
- Kulsrud, R. M., & Cesarsky, C. J. 1971, *Astrophys. Lett.*, 8, 189
- Li, M., Bryan, G. L., & Ostriker, J. P. 2017, *ApJ*, 841, 101
- Martin, C. L. 2005, *ApJ*, 621, 227
- Martizzi, D., Fielding, D., Faucher-Giguère, C.-A., & Quataert, E. 2016, *MNRAS*, 459, 2311
- Moster, B. P., Naab, T., & White, S. D. M. 2013, *MNRAS*, 428, 3121
- Murray, N., Quataert, E., & Thompson, T. A. 2005, *ApJ*, 618, 569
- Naab, T., & Ostriker, J. P. 2017, *ARA&A*, 55, 59
- Ostriker, E. C., McKee, C. F., & Leroy, A. K. 2010, *ApJ*, 721, 975
- Ostriker, E. C., & Shetty, R. 2011, *ApJ*, 731, 41
- Prochaska, J. X., Werk, J. K., Worseck, G., et al. 2017, *ApJ*, 837, 169
- Proga, D., Jiang, Y.-F., Davis, S. W., Stone, J. M., & Smith, D. 2014, *ApJ*, 780, 51
- Putman, M. E., Peek, J. E. G., & Joungh, M. R. 2012, *ARA&A*, 50, 491
- Recchia, S., Blasi, P., & Morlino, G. 2016, *MNRAS*, 462, 4227
- Rodríguez-Puebla, A., Primack, J. R., Avila-Reese, V., & Faber, S. M. 2017, *MNRAS*, 470, 651
- Ruszkowski, M., Yang, H.-Y. K., & Zweibel, E. 2017, *ApJ*, 834, 208
- Salem, M., & Bryan, G. L. 2014, *MNRAS*, 437, 3312
- Salem, M., Bryan, G. L., & Hummels, C. 2014, *ApJL*, 797, L18
- Scannapieco, E., & Brüggen, M. 2015, *ApJ*, 805, 158
- Simpson, C. M., Pakmor, R., Marinacci, F., et al. 2016, *ApJL*, 827, L29
- Somerville, R. S., & Davé, R. 2015, *ARA&A*, 53, 51
- Thompson, T. A., Quataert, E., Zhang, D., & Weinberg, D. H. 2016, *MNRAS*, 455, 1830
- Tumlinson, J., Peebles, M. S., & Werk, J. K. 2017, *ARA&A*, 55, 389
- Uhlig, M., Pfrommer, C., Sharma, M., et al. 2012, *MNRAS*, 423, 2374
- Veilleux, S., Cecil, G., & Bland-Hawthorn, J. 2005, *ARA&A*, 43, 769
- Wang, B. 1995, *ApJ*, 444, 590
- Werk, J. K., Prochaska, J. X., Tumlinson, J., et al. 2014, *ApJ*, 792, 8
- Wiener, J., Oh, S. P., & Guo, F. 2013, *MNRAS*, 434, 2209
- Wiener, J., Pfrommer, C., & Peng Oh, S. 2017, *MNRAS*, 467, 906
- Zhang, D., Davis, S. W., Jiang, Y.-F., & Stone, J. M. 2017a, *ArXiv e-prints*, arXiv:1708.02946
- Zhang, D., Thompson, T. A., Quataert, E., & Murray, N. 2017b, *MNRAS*, 468, 4801
- Zirakashvili, V. N., Breitschwerdt, D., Ptuskin, V. S., & Voelk, H. J. 1996, *A&A*, 311, 113
- Zweibel, E. G. 2017, *Physics of Plasmas*, 24, 055402